Spring 2013

Development and validation of a sharp interface cavitation model

Thad Jefferson Michael
University of Iowa

DEVELOPMENT AND VALIDATION OF A SHARP INTERFACE CAVITATION MODEL

by

Thad Jefferson Michael

An Abstract

Of a thesis submitted in partial fulfillment
of the requirements for the Doctor of
Philosophy degree in Mechanical Engineering
in the Graduate College of
The University of Iowa

May 2013

Thesis Supervisors: Professor Frederick Stern
Adjunct Associate Professor Jianming Yang

ABSTRACT

A sharp interface cavitation model has been developed for computational fluid dynamics. A phase change model based on a simplification of the Rayleigh-Plesset equation is combined with a second-order volume-of-fluid method with a constructed level set function in an incompressible fluid dynamics model.

The semi-implicit phase change model predicts the mass flux between liquid and vapor phases based on the difference between the local pressure at the interface and the vapor pressure at the ambient conditions. The mass flux between phases determines the volume source strength and jump velocities at the interface.

To prevent difficulties computing derivatives near the interface, two separate velocity fields from the momentum equation are solved considering the interface velocity jump. The interface velocity jump is extended into the liquid and vapor domains using a fast marching method.

A description of the mathematical and numerical models is included, as well as an explanation and derivation of the phase change model. Hypothetical vapor bubble problems are demonstrated to test the components of the model. Finally, cavity evolution on a hydrofoil is computed for a range of parameters.

Abstract Approved: _____
Thesis Supervisor

_____
Title and Department

_____
Date

_____
Thesis Supervisor

_____
Title and Department

_____
Date

DEVELOPMENT AND VALIDATION OF A SHARP INTERFACE CAVITATION MODEL

by

Thad Jefferson Michael

A thesis submitted in partial fulfillment
of the requirements for the Doctor of
Philosophy degree in Mechanical Engineering
in the Graduate College of
The University of Iowa

May 2013

Thesis Supervisors: Professor Frederick Stern
Adjunct Associate Professor Jianming Yang

Graduate College
The University of Iowa
Iowa City, Iowa

CERTIFICATE OF APPROVAL

_____

PH.D. THESIS

_____

This is to certify that the Ph.D. thesis of

Thad Jefferson Michael

has been approved by the Examining Committee
for the thesis requirement for the Doctor of Philosophy
degree in Mechanical Engineering at the May 2013 graduation.

Thesis Committee: _____
Frederick Stern, Thesis Supervisor

_____
Jianming Yang, Thesis Supervisor

_____
Pablo Carrica

_____
George Constantinescu

_____
Ching-Long Lin

To my wife, who followed me to Iowa.

That cavitation will be the cause of trouble in the future is, I think, certain.

Sydney W. Barnaby, *INA Trans.* Vol. 39, 1898

ACKNOWLEDGMENTS

I would like to express my thanks to my advisors, Professor Stern and Dr. Yang, who have helped me find my way through many challenges in the course of this research. I would also like to thank Professor Pablo Carrica for his generous advice and support. Dr. Sung-Eun Kim of NSWC Carderock Division also gave me excellent advice. I sincerely appreciate the time and effort my committee members have devoted to this work. And, I thank my coworkers for their patience and support throughout this effort.

This work has been made possible by funding from the US Department of Defense Science, Mathematics, and Research for Transformation (SMART) Program, and the Naval Surface Warfare Center, Carderock Division In-house Laboratory Independent Research (ILIR) and Extended Term Training (ETT) Programs.

ABSTRACT

A sharp interface cavitation model has been developed for computational fluid dynamics. A phase change model based on a simplification of the Rayleigh-Plesset equation is combined with a second-order volume-of-fluid method with a constructed level set function in an incompressible fluid dynamics model.

The semi-implicit phase change model predicts the mass flux between liquid and vapor phases based on the difference between the local pressure at the interface and the vapor pressure at the ambient conditions. The mass flux between phases determines the volume source strength and jump velocities at the interface.

To prevent difficulties computing derivatives near the interface, two separate velocity fields from the momentum equation are solved considering the interface velocity jump. The interface velocity jump is extended into the liquid and vapor domains using a fast marching method.

A description of the mathematical and numerical models is included, as well as an explanation and derivation of the phase change model. Hypothetical vapor bubble problems are demonstrated to test the components of the model. Finally, cavity evolution on a hydrofoil is computed for a range of parameters.

TABLE OF CONTENTS

LIST OF TABLES

LIST OF FIGURES

INTRODUCTION

This thesis describes past cavitation modeling efforts and the development of a new cavitation modeling method for sharp interface two phase methods. CFDShip-Iowa v6.2 has been modified to include a new cavitation phase change model for sharp interfaces and supporting methods, including the ghost fluid method for using a high-order convection method with a field that includes a velocity jump and a fast marching method for extending a scalar variable from the interface.

After a discussion of the significance of cavitation and of previous modeling efforts, the mathematical and numerical basis and implementation is described. Simulations of cavitation bubbles and cavitating hydrofoils are described for verification and validation.

Background

Cavitation is the term for the change of state from liquid to vapor when it is caused by a low pressure region within a flow field. In contrast, the term boiling is used when a fluid changes from liquid to vapor due to a high temperature. Both are similar phenomena and have the same physical mechanisms—in both cases the liquid reaches a combination of pressure and temperature that dictate a change of state to vapor. In cavitation, the local pressure drops below the vapor pressure at the ambient temperature. In boiling, the vapor pressure at the local temperature rises above the ambient pressure. Therefore, in the case of boiling, the surrounding heat flux is critical while the local pressure is relatively unimportant, whereas in cavitation the heat flux is relatively unimportant but the pressure field is critical.

Figure 1 shows sheet cavitation on a hydrofoil. Flow is from left to right. Some of the cavity is being shed downstream. The cavity is caused by the low pressure induced on the upper surface by the angle of attack.

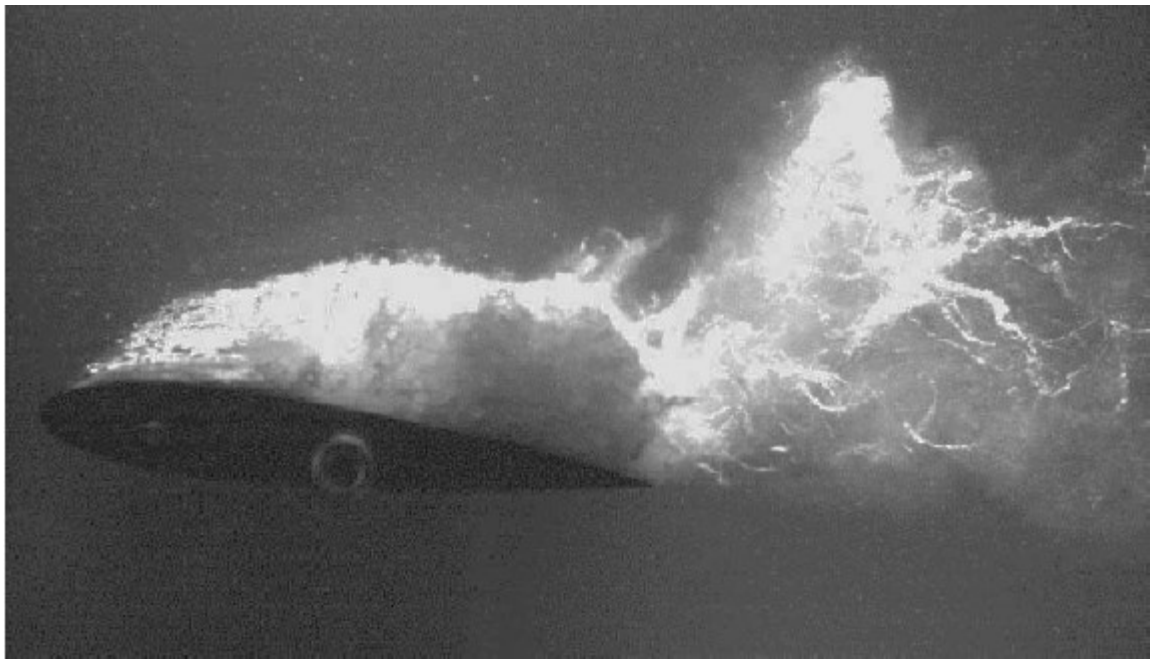

Figure 1: Sheet cavitation on a hydrofoil (Arndt *et al.*, 2005).

Significance of Cavitation

Cavitation can be detrimental to the performance of lifting surfaces and the materials used to build them. In the marine environment, cavitation often occurs on propellers, on rudders, and in pumps. Cavitation is also a problem in other areas, including water turbines and many types of pumps.

When a large part of the surface of any lifting surface, such as a propeller or pump rotor, is covered by a vapor, the pressure cannot be reduced further. For lifting surfaces designed for wetted operation, this sets an upper limit on the amount of lift that can be produced. In pumps, the expanding vapor acts as an obstruction which chokes the flow, further reducing performance.

Furthermore, the collapse of cavitation bubbles is so violent that it will cause surface pitting, even in steel. This pitting is called cavitation erosion and, like soil

erosion, can remove a significant amount of material over time. This can cause degraded lifting performance and structural failure.

Figure 2 shows the destructive effects of cavitation erosion on the rudder of a ship. The paint has been worn away and the bare metal is exposed over a large area. The cavitation shown here is a sheet cavity caused by an angle of attack on the rudder due to the swirl from the propeller wake.

Figure 2: Cavitation erosion of a ship rudder (Shen *et al.* 1997).

Cavitation Modeling

Potential flow cavitation models have been successfully applied to propellers by Lee (1979) and Kerwin, *et al.* (1987). These models use lifting surface theory or potential panels to represent the blade surface. Cavities are modeled with sources or additional panels.

Past research in cavitation modeling with viscous codes has relied primarily on homogenous mixture models. Phase change models for use with the mixture model were

developed by Merkle *et al.* (1998) and Kunz *et al.* (1999) and are still commonly used. A slightly more recent model by Singhal *et al.* (2002) is based on similar principles and adds the ability to model non-condensable gas within the bubbles. Recent computations by and Kim *et al.* (2008, 2010a, 2010b) and Bensow *et al.* (2008) using these models, or similar ones, has shown good comparison with hydrofoil and propeller experiments.

The feasibility of using a sharp interface model for phase change has been demonstrated for the case of film boiling by Son and Dhir (2007) and Gibou *et al.* (2007). This research seeks to apply similar techniques to the problem of cavitation. Cavitation may be a more difficult problem than boiling because of the close coupling between the pressure solution and the phase change rate which is not present in boiling problems.

Hydrofoil Experiments and Calculations

A hydrofoil with the NACA 66 (MOD) thickness form (Abbott and Von Doenhoff, 1959), a=0.8 mean line, with 9 percent thickness and 2 percent camber was tested by Shen and Dimotakis (1989) in a water tunnel in both cavitating and non-cavitating conditions, measuring lift, drag, cavity length, and surface pressure at several locations. Four angles of attack were measured and photographs are available of some conditions. All measurements were at Reynolds numbers of at least 1×10^6. These measurements are particularly relevant for marine propellers which often use the same thickness distribution. These measurements have been used for validation by several researchers, including Singhal *et al.* (2002), Senocak and Shyy (2004a), and Kim *et al.* (2010a), all using homogeneous mixture models. Figure 3 from Kim *et al.* (2010a) shows the predicted cavity shape at a four degree angle of attack with a cavitation number of 0.91. The cavitation number is defined like the pressure coefficient:

$$\sigma = \frac{p_{vap}}{\frac{1}{2}\rho_l U_\infty^2} \qquad (1)$$

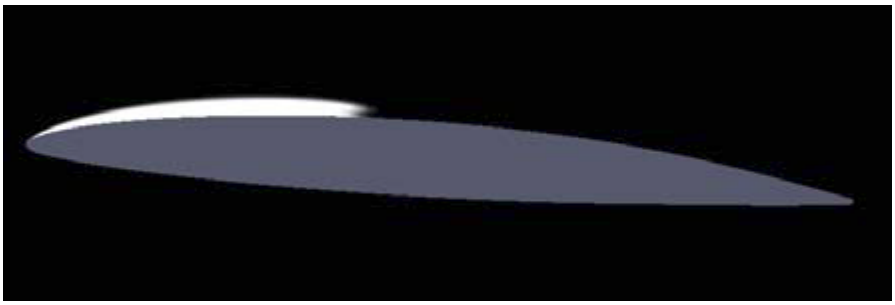

Figure 3: Predicted sheet cavity on a NACA-66 hydrofoil at 4 deg. angle of attack at σ=0.91 (Kim *et al.* 2010a).

Hydrofoils with the NACA 0015 (Abbott and Von Doenhoff, 1959) thickness form have been measured by Kato *et al.* (1978), Kjeldsen *et al.* (2000), Wosnik and Milosevic (2005), and Cervone *et al.* (2006). Measurements were typically at Reynolds numbers of at least 3×10^5. Many researchers have compared computational results with these measurements including Kubota *et al.* (1992), Hosangadi and Ahuja (2005), Kim and Brewton (2008), Kim and Schroeder (2010b), and Koop (2008).

A hydrofoil with a varying angle of attack was tested in by Foeth (2008). The foil was designed to produce a cavity near the center of the span, with shedding occurring at the same location at certain flow conditions. The foil has a varying angle of attack across the span of 11 degrees and is therefore called the Twist-11 foil. Pressure and velocity data were collected at midspan as were a large number of photographs. Data for this foil also appears in Foeth *et al.* (2006) and Foeth *et al.* (2008). The foil has a NACA 0009 section without camber. The sections of the foil are rotated about 0.75 chord according to the equation

$$\alpha = 11(2y^3 - 3y^2 + 1) + \alpha_{wall} \qquad (2)$$

where α is the rotation angle in degrees, y is the fraction of span and, for this case, α_{wall} is -3 degrees. The foil is shown in Figure 4.

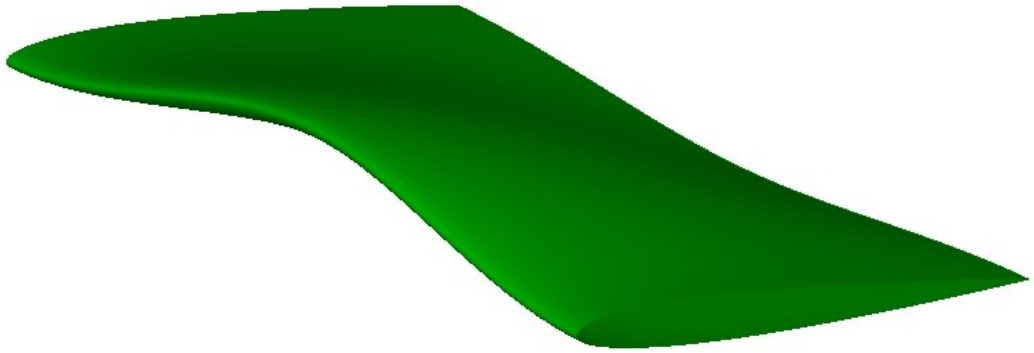

Figure 4: Twist-11 hydrofoil.

The Twist-11 foil was used for computational validation by Koop (2008) and Bensow *et al.* (2008).

Objective

The objective of this thesis is to develop and demonstrate a sharp interface cavitation model, including both the phase change rate model and the necessary models and methods to support the normal velocity jump across the interface. Simple bubble calculations and the NACA 66 hydrofoil case will be used for validation.

Approach

CFDShip-Iowa v6.2 has been modified to include a cavitation phase change model. The level set and volume of fluid sharp interface models are already included, but there are no provisions for mass transfer between phases, volume sources, or the associated discontinuity in velocity normal to the interface.

A phase change model based on the Rayleigh-Plesset equation for bubble dynamics has been developed following other researchers, but without assuming bubble size or number as done in the homogenous mixture models. In this research, the bubbles are computed directly so the equation for the rate of growth of the bubble radius can be applied directly to the interface velocity.

The Poisson equation for pressure has been modified to include the volume source due to mass flux between phases of different densities. The strength of the source is determined by the phase change rate. The phase change rate can be computed in a semi-implicit fashion through modifications to the Poisson solution.

A ghost fluid method has been implemented to allow the existing momentum solver to be applied to flow fields containing a jump in the normal velocity. This is accomplished by dividing the flow field into separate fields for each phase and extending the velocities across the interface to produce separate continuous fields, applying the momentum solver, and then recombining those fields.

A boundary condition will be developed to support the need for a velocity inlet over the forward part of the O-grid around a foil and a pressure outlet downstream.

CAVITATION MODELING

Many computational investigations into cavitation have been made in recent years. Modeling efforts can be divided into two broad categories: discrete bubble models and vapor transport models.

Discrete bubble models typically include the effects of the surrounding fluid on the bubbles, but do not include the effect of the bubble on the fluid. Discrete bubble models are best suited to cavitation inception, when only a small number of bubbles are required.

Vapor transport models are best suited to large scale cavitation, such as the sheet cavitation that often occurs on propellers and rudders. These models include two-way interaction between the phases. This is the type of modeling proposed in the present effort.

Modeling cavitation consists of two distinct parts: the modeling of the two phases, as in a free surface code, and the modeling of the mass transfer between the phases. In cavitation, the mass transfer between liquid and vapor phases is driven by pressure. This is in contrast to boiling, in which the phase change is driven by temperature.

Two Phase Models

Two common types of two phase models are homogenous mixture models and sharp interface models. They differ in the treatment of the contents of cells containing both phases.

Most recent cavitation modeling efforts have used homogenous mixture models, in which the contents of individual cells are considered uniform. This approach is well suited to modeling large numbers of small bubbles; bubbles that are much smaller than one cell. The disadvantage of this approach is that for large cavities, larger than one cell, the vapor fraction is diffused across neighboring cells by the transport model.

The present cavitation modeling effort is different in that the vapor and liquid are modeled as distinct phases separated by an interface. In sharp interface models, the interface is not diffused by advection. The model maintains a sharp interface. Naturally, this is only appropriate when the bubble size is at least on the order of a few cells. CFDShip-Iowa version 6 already has level set, volume-of-fluid, and coupled level set and volume-of-fluid two phase models (Wang *et al.* 2009).

Nguyen *et al.* (2001) applied the level set method to incompressible flame fronts as an extension of the ghost fluid method. Son and Dhir (2007) used level set method to model film boiling on a surface, a related phase change problem. Gibou, *et al.* (2007) also applied the level set method to phase change due to boiling.

Phase Change Models

There are three general categories of phase change models used for cavitation. The barotropic models, equilibrium models, and models derived from a simplified version of the Rayleigh-Plesset equation. This section will briefly discuss the advantages and disadvantages of each type.

Barotropic Model - Vapor Pressure

If the pressure is greater than vapor pressure, then the fluid is liquid, otherwise vapor.

$$\rho = \begin{cases} \rho_l \text{ if } p > p_{vap} \\ \rho_v \text{ if } p < p_{vap} \end{cases} \tag{3}$$

where ρ_l is the density of liquid water, ρ_v is the density of water vapor, and p_{vap} is the vapor pressure of water at the ambient temperature.

For stability, a smoothed function can be used, with the slope based on the speed of sound. There are several variations, for example Delannoy and Kueny (1990). The main criticism of this method is that it cannot capture the baroclinic torque due to the

difference between the pressure and density gradients (Kim and Brewton, 2008, and others).

Equilibrium Model - Energy

This method requires minimal modeling of the phase change rate. It requires the solution of the energy equation. An equation of state for water is used, with the energy absorbed or released by phase change creating local temperature gradients which control the rate of phase change.

$$\rho = \rho(p, T) \tag{4}$$

For examples, see Gibou *et al.* (2007) and Koop (2008). Few researchers have employed this method because has a high computational cost and the local temperature gradient has been shown to have little effect in the all but the smallest bubbles (Franc and Michel 2004).

Rayleigh-Plesset-based Models – Pressure

A number of researchers have derrived equations for the phase change rate from the Rayleigh-Plesset equation for bubble dynamics (Plesset and Prosperetti, 1977). This is the approach used in this research and a full derivation of the model to be used is included in a later section. The Rayleigh-Plesset equation assumes a bubble of saturated vapor growing in an infinite, viscous, incompressible medium. Heat exchange is neglected.

Merkle *et al.* (1998) used separate equations for condensation and evaporation.

$$\dot{m}^{+} = \frac{C_{cond}\rho_v\alpha_l min\left[0, p - p_{vap}\right]}{\frac{1}{2}\rho_l U_\infty^2 t_\infty} \tag{5}$$

$$\dot{m}^{-} = \frac{C_{evap}\rho_v\alpha_l max\left[0, p - p_{vap}\right]}{\frac{1}{2}\rho_l U_\infty^2 t_\infty} \tag{6}$$

where $C_{prod} = 10^5$ and $C_{dest} = 0.2$, $\dot{m}$ is the mass flux between phases, and α_l is the volume fraction of liquid. The quantities U_∞ and t_∞ are characteristic values of the velocity and time, respectively.

The model reported by Kunz *et al.* (1999) uses separate equations for evaporation and condensation. The transformation of liquid to vapor is modeled similar to Merkle *et al.* (1998).

$$\dot{m}^- = \frac{C_{evap}\rho_v\alpha_l min[0, p - p_{vap}]}{(1/2\,\rho_l U_\infty^2)t_\infty} \tag{7}$$

The transformation of vapor to liquid is based on a simplified form of the Ginzburg-Landau potential.

$$\dot{m}^+ = \frac{C_{cond}\rho_v(\alpha_l - \alpha_{ng})^2(1 - \alpha_l - \alpha_{ng})}{t_\infty} \tag{8}$$

The constants are $C_{prod} = C_{dest} = 0.2$ and the term α_{ng} is the volume fraction of non-condensable gas, *e.g.* air. Interestingly, the condensation rate is independent of pressure.

Singhal *et al.* (2002) developed a model with rates of evaporation and condensation derived from a first-order approximation of the Rayleigh-Plesset equation, ignoring acceleration, surface tension, and viscous effects. The rate of evaporation is approximated by

$$R_e = 0.02\frac{V_{ch}}{\sigma}\rho_l\rho_v\sqrt{\frac{2(p_{vap} - p)}{3\rho_l}}\left(1 - \alpha_v\frac{\rho_v}{\rho_m}\right) \tag{9}$$

And, the rate of condensation is approximated by

$$R_c = 0.01\frac{V_{ch}}{\sigma}\rho_l\rho_v\sqrt{\frac{2(p - p_{vap})}{3\rho_l}}\left(\alpha_v\frac{\rho_v}{\rho_m}\right) \tag{10}$$

The difference in constants indicates that rate of evaporation is expected to be twice the rate of condensation for similar conditions when the pressure difference is reversed. The characteristic velocity, V_{ch}, is approximated by the local turbulence

intensity and σ is the surface tension. The source of the surface tension term in these equations is not the Rayleigh-Plesset equation, but instead an assumed relationship for the characteristic bubble radius. A version accounting for the presence of non-condensable gasses is also available.

A comparison of these cavitation models by Senocak and Shyy (2004a) is reproduced in Figure 5. The figure shows that, within the resolution of the experimental data for the NACA 66 hydrofoil (Shen and Dimotakis, 1989), the Rayleigh-Plesset-based models yield similar results. Model-1 is Merkle *et al.* (1998), Model-2 is Kunz *et al.* (1999), and Model-3 is Singhal *et al.* (2002).

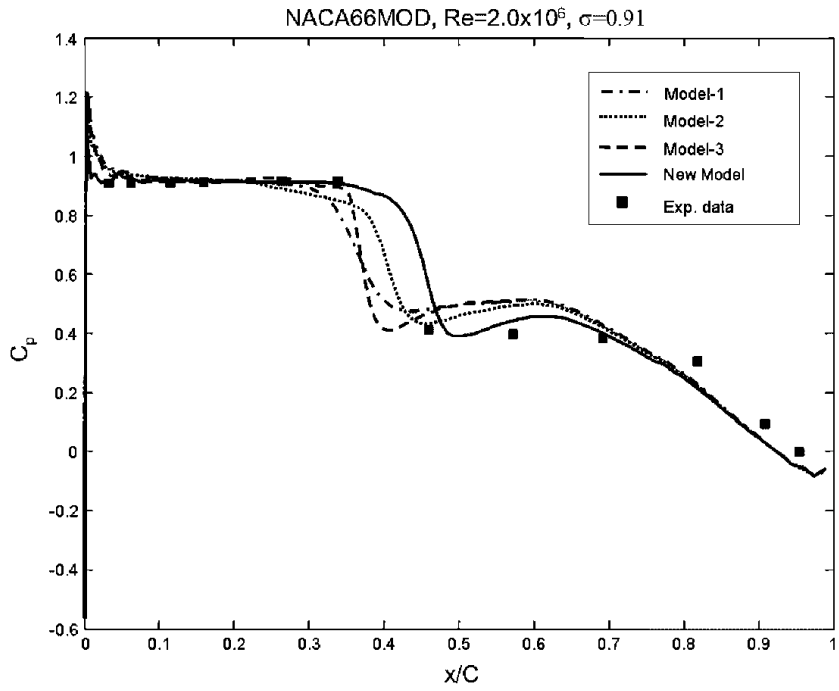

Figure 5: Comparison of surface pressure distributions with various phase change models (Senocack and Shyy, 2004a).

Senocack and Shyy give an excellent explanation of the origins and interpretations of the terms in the phase change rate equations. They also developed their own version, which has terms similar to Merkle *et al.* (1998), but is not widely used.

Rankine-Hugoniot Jump Conditions

The Rankine-Hugoniot jump conditions satisfy mass and momentum conservation at the interface

$$\left[\rho_f \left(\boldsymbol{u}_{f_N} - \boldsymbol{U}_N\right)\right] = 0 \tag{11}$$

$$\left[\rho_f \left(\boldsymbol{u}_{f_N} - \boldsymbol{U}_N\right)^2 + p\right] = 0 \tag{12}$$

where $\boldsymbol{u}_{fN}$ and $\boldsymbol{U}_N$ are the normal components of the fluid and interface velocities, respectively, and [X] denotes the difference, or jump, in quantity X across the interface. The difference between the fluid and interface velocities is due to the mass transfer between phases and the change in density. The mass flux between phases can be defined

$$\dot{m} = \rho_l \left(U_N - u_{l_N}\right) = \rho_v \left(U_N - u_{v_N}\right) \tag{13}$$

noting that

$$[\dot{m}] = 0 \tag{14}$$

as required by mass conservation.

Velocity Jump at the Interface

At the interface, continuity requires

$$\boldsymbol{U} = \boldsymbol{u}_l + \frac{\dot{m}\boldsymbol{n}}{\rho_l} = \boldsymbol{u}_v + \frac{\dot{m}\boldsymbol{n}}{\rho_v} \tag{15}$$

where the subscripts l and v represent the liquid and vapor phases, respectively. Therefore, the velocity jump at the interface is

$$[\boldsymbol{u}] = \boldsymbol{u}_l - \boldsymbol{u}_v = \frac{\dot{m}\boldsymbol{n}}{\rho_v} - \frac{\dot{m}\boldsymbol{n}}{\rho_l} = \dot{m}\left(\frac{1}{\rho_v} - \frac{1}{\rho_l}\right)\boldsymbol{n} = \dot{m}\left[\frac{1}{\rho}\right]\boldsymbol{n} \tag{16}$$

Pressure Jump at the Interface

The pressure jump at the interface satisfies the conservation of momentum across the interface. From substituting Equation (13) in to Equation (12),

$$\left[\frac{\dot{m}^2}{\rho} + p\right] = 0 \tag{17}$$

This can be rearranged to show that the pressure jump at the interface is

$$[p] = -\dot{m}^2\left[\frac{1}{\rho}\right] \tag{18}$$

Volume-of-Fluid Method with Phase Change

The value of the volume-of-fluid (VOF) scalar, F, represents the fraction of the cell that is filled with liquid. Without phase change, the scalar is advanced by the local fluid velocity, $\boldsymbol{u}_f$, while satisfying the equation

$$\frac{\partial F}{\partial t} + \boldsymbol{u}_f \cdot \nabla F = 0 \tag{19}$$

where the local fluid velocity and the interface velocity are the same. When phase change is included, the VOF function is advanced by the interface velocity while solving the equation

$$\frac{\partial F}{\partial t} + \boldsymbol{U} \cdot \nabla \phi = 0 \tag{20}$$

where $\boldsymbol{U}$ is the interface velocity. With mass transfer between phases, the interface velocity is the combination of the fluid velocity, $\boldsymbol{u}_f$, and the relative velocity due to phase change such that

$$\boldsymbol{U} = \boldsymbol{u}_f + \frac{\dot{m}\boldsymbol{n}}{\rho_f} \tag{21}$$

where $\dot{m}$ is the mass flux across the interface as determined by a phase change model.

For typical cavitation problems in water, the interface velocity is always close to the liquid velocity and it is often more expedient to use the liquid velocity field,

determined by the ghost fluid method, to advect the interface. However, in this research the more rigorous method of using the interface velocity has been chosen. The VOF is advected by substituting the interface velocity for the fluid velocity in the method described by Wang *et al.* (2012).

Level Set Equations with Phase Change

The value of the level set function, ϕ, is defined as zero at the interface. In the common implementation of the level set method without phase change, the function is advanced by the local fluid velocity, $\boldsymbol{u}_f$, while solving the equation

$$\frac{\partial \phi}{\partial t} + \boldsymbol{u}_f \cdot \nabla \phi = 0 \tag{22}$$

The level set equation can be modified in the same way as the VOF equation tu use the interface velocity for advection. In this research, the level set function is recomputed from the volume-of-fluid scalar at each time step.

Phase Change Rate

The rate of phase change, or mass flux between phases, determines the velocity of the interface relative to the liquid and vapor phases. Franc and Michel (2004) showed that the rate of heat transfer in water is sufficiently high that it can be neglected for most practical problems. If the energy equation were to be solved accurately in this case, very small time steps would be required to adequately capture the heat transfer and a very fine grid to capture the temperature gradients at the interface. Therefore, a phase change model based on the primary governing quantity, pressure, is desired. This requires some assumptions. Models based on the Rayleigh-Plesset equation have been shown to produce satisfactory results, as described earlier.

The Rayleigh-Plesset equation describes the evolution of a three-dimensional, spherical bubble filled with saturated vapor and subject to uniform pressure variation.

$$\rho_l\left(R\ddot{R}+\frac{3}{2}\dot{R}^2\right)=p_{vap}-p_\infty(t)+p_{g0}\left(\frac{R_0}{R}\right)^{3\gamma}-\frac{2S}{R}-4\mu\frac{\dot{R}}{R} \qquad (23)$$

where p_{g0} is the initial partial pressure of non-condensable gasses, R_0 is the initial radius of the bubble, and S is the surface tension (Plesset and Prosperetti, 1977). The third term on the right hand side represents the effect of the non-condensable gasses. The last two terms on the right represent the effects of surface tension and viscosity, respectively. The surface tension can be neglected for all but the smallest bubbles and the viscous effects can be neglected for the Reynolds numbers of interest in ship flows.

If we note that the time-varying term on the right can be expressed

$$R\ddot{R}+\frac{3}{2}\dot{R}^2=\frac{1}{2\dot{R}R^2}\frac{d\left(\dot{R}^2R^3\right)}{dt} \qquad (24)$$

Then, dropping the non-condensable gas, surface tension, and viscosity terms and integrating with respect to time yields:

$$\frac{dR}{dt}=\sqrt{\frac{2}{3}\frac{\left(p_\infty-p_{vap}\right)}{\rho_l}\left(1-\left(\frac{R_0}{R}\right)^3\right)} \qquad (25)$$

The cube of the initial radius, R_0, represents the volume of non-condensable gasses present in the nuclei before phase change caused the bubble to grow. Hence, the ratio of the initial radius to the instantaneous radius of a cavitation bubble will be small once cavitation growth begins until just before bubble collapse, both below the expected resolution of the flow solver. Therefore, the cube of the ratio can be neglected, leaving

$$\frac{dR}{dt}=\sqrt{\frac{2}{3}\frac{\left(p_\infty-p_{vap}\right)}{\rho_l}} \qquad (26)$$

This equation describing the time rate of change of a bubble radius subject to a pressure field is the foundation of several mass-transfer phase-change models where the local pressure replaces the far field pressure in the equation above.

In the volume of fluid and level set methods, bubbles must be larger than a cell to be tracked. When the interface is convected in the volume of fluid method, it is modeled as a plane in each cell. If the radius is sufficiently large, then the rate of change of the radius with respect to time can be approximated by the advancement of the planer interface in the direction normal to the interface during a time step. That is, the velocity of the interface relative to the liquid can be approximated as

$$\frac{\dot{m}\boldsymbol{n}}{\rho_l} = \sqrt{\frac{2}{3}\frac{(p - p_{vap})}{\rho_l}}\,\boldsymbol{n} \tag{27}$$

so that

$$\dot{m} = \sqrt{\frac{2}{3}\rho_l(p - p_{vap})} \tag{28}$$

OVERVIEW OF AND IMPLEMENTATION IN CFDSHIP-IOWA V6.2

The unsteady, three-dimensional, incompressible Navier-Stokes equations are solved in the orthogonal curvilinear coordinate system (Suh *et al.*, 2011):

$$\nabla(\mathrm{i})(u_i) = 0 \tag{29}$$

$$\begin{aligned}\frac{\partial u_i}{\partial t} + \nabla(\mathrm{j})\left(u_i u_j\right) - \frac{1}{\rho}\nabla_j \tau_\psi \\ = -\frac{1}{\rho}\frac{\partial p}{\partial \xi_i} + g_i + H_j(i)\left(u_j u_j - \frac{\tau_{ij}}{\rho}\right) \\ - H_i(j)\left(u_i u_i - \frac{\tau_{ij}}{\rho}\right)\end{aligned} \tag{30}$$

where u_i and g_i (i = 1, 2, 3) are the velocity and the gravity in the orthogonal coordinate ξ_i direction, respectively, and $h_i = \partial x_i/\partial \xi_i$ with x_i denoting a Cartesian coordinate. In addition,

$$H_i(j) = \frac{1}{h_i h_j}\frac{\partial h_i}{\partial \xi_j} \tag{31}$$

$$\nabla(\mathrm{i})(\cdot) = \frac{1}{J}\frac{\partial}{\partial \xi_i}\left(\left(\frac{J}{h_i}\right)\right) \tag{32}$$

The Jacobian of the coordinate transformation is defined as $J = h_i h_j h_k$. The viscous stress tensor τ_{ij} is defined as follows:

$$\tau_{ij} = \mu\left(\frac{\partial u_i}{\partial \xi(j)} + \frac{\partial u_j}{\partial \xi(i)} - u_j H_j(i) + 2u_l H_i(l)\delta_{ij}\right) \tag{33}$$

where $\partial\xi(i) = h_i\partial\xi_i$, μ is the dynamic viscosity and δ_{ij} is the Kronecker delta function.

Numerical Method

A marker-and-cell (MAC) grid is adopted for stability. Velocities are defined at cell faces while scalar quantities, e.g. pressure, level set, VoF, are defined at cell centers.

The Navier-Stokes equations are advanced in time with a first order implicit Euler method. A Poisson equation for pressure enforces continuity. A semi-coarsening

multigrid solver from the HYPRE library (Falgout *et al.*, 2006) is used to solve the pressure Poisson equation. For cavitation modeling, a source term is added to the Poisson equation representing the velocity divergence created by the volume source. The solution method is:

Step 1, predictor

$$\frac{u_i^* - u_i^n}{\Delta t} = A_i^n + C_i^{n+1} - \mathrm{Grad}_i(p^n) \tag{34}$$

Step 2, pressure Poisson equation

$$\frac{\partial}{\partial x_i}\mathrm{Grad}_i(p^{n+1}) = \frac{1}{\Delta t}\left(\frac{\partial u_i^*}{\partial x_i} + \underbrace{\dot{m}\left(\frac{1}{\rho_v} - \frac{1}{\rho_l}\right)}_{source\ term}\right) \tag{35}$$

$\mathrm{Grad}_i(p)$ is collocated with the velocity components and incorporates the jump conditions due to surface tension and gravity (Yang and Stern 2009).

Step 3, second corrector, adds the new pressure gradient

$$\frac{u_i^{n+1} - u_i^*}{\Delta t} = -\mathrm{Grad}_i(p^{n+1}) \tag{36}$$

A and ***C*** are terms are treated explicitly and implicitly, respectively

$$\boldsymbol{A} = -\bar{\boldsymbol{u}} \cdot \nabla \bar{\boldsymbol{u}} + \frac{1}{\rho}\nabla \cdot [\mu(\nabla \bar{\boldsymbol{u}})^{\mathrm{T}}]] \tag{37}$$

$$\boldsymbol{C} = \frac{1}{\rho}\nabla \cdot [\mu(\nabla \bar{\boldsymbol{u}})]] \tag{38}$$

When continuity is satisfied, the phase change volume source term in the Poisson equation will balance the velocity divergence.

The ghost fluid method is "wrapped" around Step 1 to allow the existing momentum method with a 5th order WENO scheme to be used on the liquid and vapor flow fields independently. Then the resulting two flow fields are combined based on the sign of the level set function. Figure 6 shows the flow of the modified code.

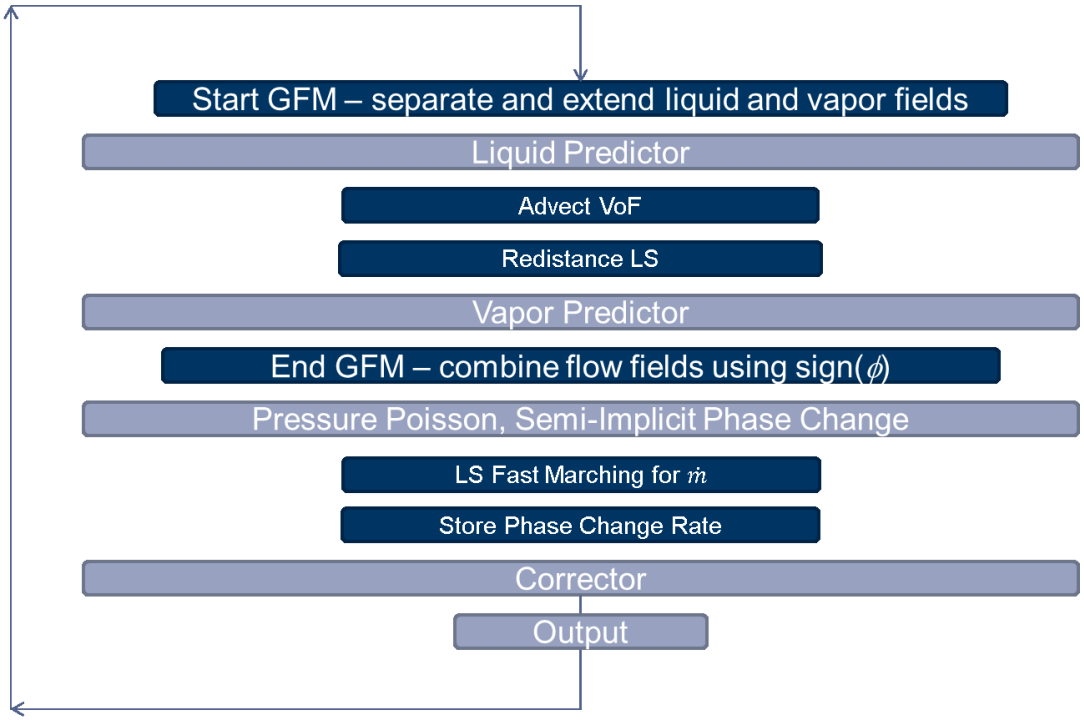

Figure 6: Flow chart describing execution of major elements of v6.2 with cavitation modeling

Semi-Implicit Linearized Phase Change Model

For stability, the pressure Poisson equation is modified to include the phase change equation semi-implicitly. To do this, the source term in Equation (35) is linearized and separated into implicit and explicit parts.

$$\dot{m}\left(\frac{1}{\rho_v}-\frac{1}{\rho_l}\right) = sign(p-p_{vap})E\sqrt{|p-p_{vap}|} \tag{39}$$

where E is the constant

$$E = \left(\frac{1}{\rho_v}-\frac{1}{\rho_l}\right)\sqrt{\frac{2}{3}\rho_l} \tag{40}$$

The square root is linearized similar to Kim and Brewton (2008)

$$sign\left(p^{n+1}-p_{vap}\right)\sqrt{\left|p^{n+1}-p_{vap}\right|}\approx\frac{p^{n+1}-p_{vap}}{\sqrt{\left|p^{n}-p_{vap}\right|}} \tag{41}$$

Now, the source term can be represented by semi-implicit and explicit parts:

$$\dot{m}\left(\frac{1}{\rho_v}-\frac{1}{\rho_l}\right)=\underbrace{\frac{E\,p^{n+1}}{\sqrt{\left|p^{n}-p_{vap}\right|}}}_{semi-implicit\ part}\underbrace{-\frac{E\,p_{vap}}{\sqrt{\left|p^{n}-p_{vap}\right|}}}_{explicit\ part} \tag{42}$$

The revised pressure Poisson equation in Step 3 is

$$\frac{\partial}{\partial x_i}\mathrm{Grad}_i(p^{n+1})-\frac{E\,p^{n+1}}{\sqrt{\left|p^{n}-p_{vap}\right|}}=\frac{1}{\Delta t}\left(\frac{\partial u_i^*}{\partial x_i}-\frac{E\,p_{vap}}{\sqrt{\left|p^{n}-p_{vap}\right|}}\right) \tag{43}$$

which determines the mass flux between phases semi-implicitly. The semi-implicit coefficient is added to the left-hand side coefficients for the Poisson solver while the explicit part is added to the right-hand side.

When the pressure and vapor pressure are equal, the denominator of both the explicit and semi-implicit terms will be zero. This is consistent with the infinite slope of the phase change rate at this point, as shown in Figure 7. To manage this situation, a minimum value for the quantity

$$\sqrt{\left|p^{n}-p_{vap}\right|} \tag{44}$$

is selected. A minimum value of 0.5 is shown in Figure 6 and used in the calculations shown later in this thesis.

The contribution of the pressure jump due to momentum conservation is at least an order of magnitude smaller than the volume source and therefore it can be treated explicitly for simplicity, using the phase change rate from the previous time step.

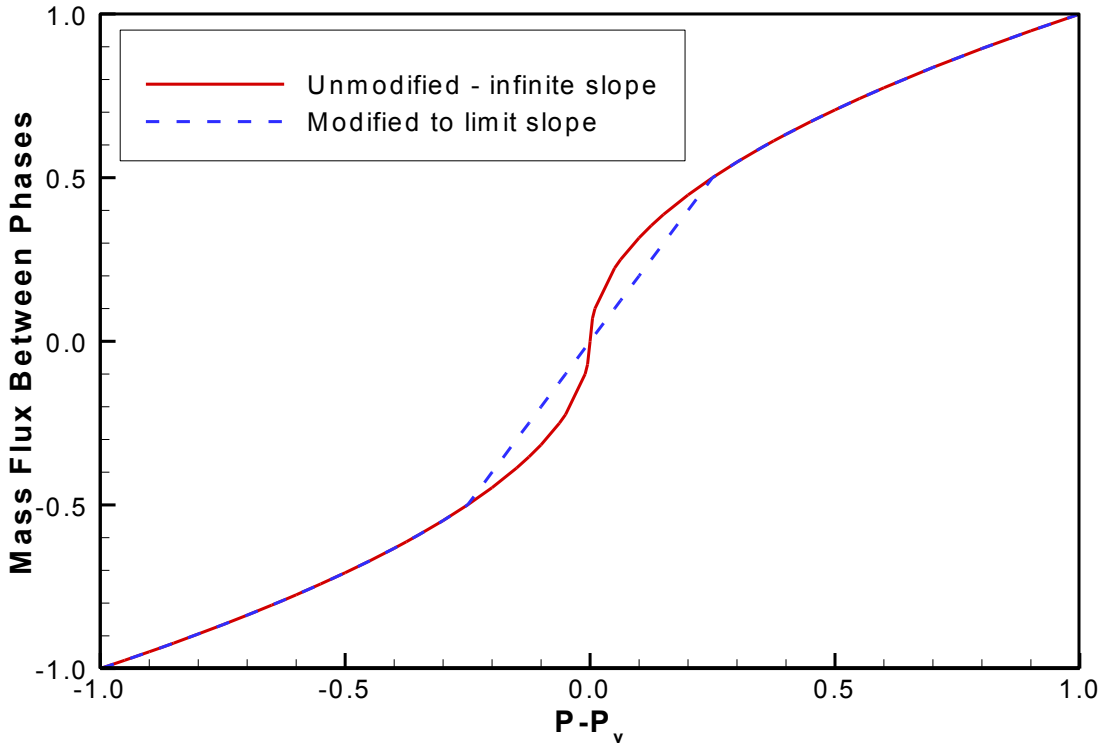

Figure 7: Phase change rate vs. pressure difference.

$$[p^{n+1}] = -(\dot{m}^n)^2 \left[\frac{1}{\rho}\right] \tag{45}$$

$$\frac{\partial}{\partial x_i}\mathrm{Grad}_i(p^{n+1}) - \frac{E\,p^{n+1}}{\sqrt{|p^n - p_{vap}|}} = \frac{1}{\Delta t}\left(\frac{\partial u_i^*}{\partial x_i} - \frac{E\,p_{vap}}{\sqrt{|p^n - p_{vap}|}}\right) - (\dot{m}^n)^2 \left[\frac{1}{\rho}\right] \tag{46}$$

The phase change rate from the previous time step is determined by preserving the pressure from the previous time step and using it to compute the rate using Equation (42), above.

Numerical Treatment of the Volume Source and Velocity Jump

Initially, the velocity jump due to phase change was treated in a discrete fashion. A velocity jump and the corresponding source were applied when two velocity points were separated by an interface, similar to the method used by Nguyen *et al.* (2001), Son and Dhir (2007), Gibou *et al.* (2007). This is illustrated in Figure 8.

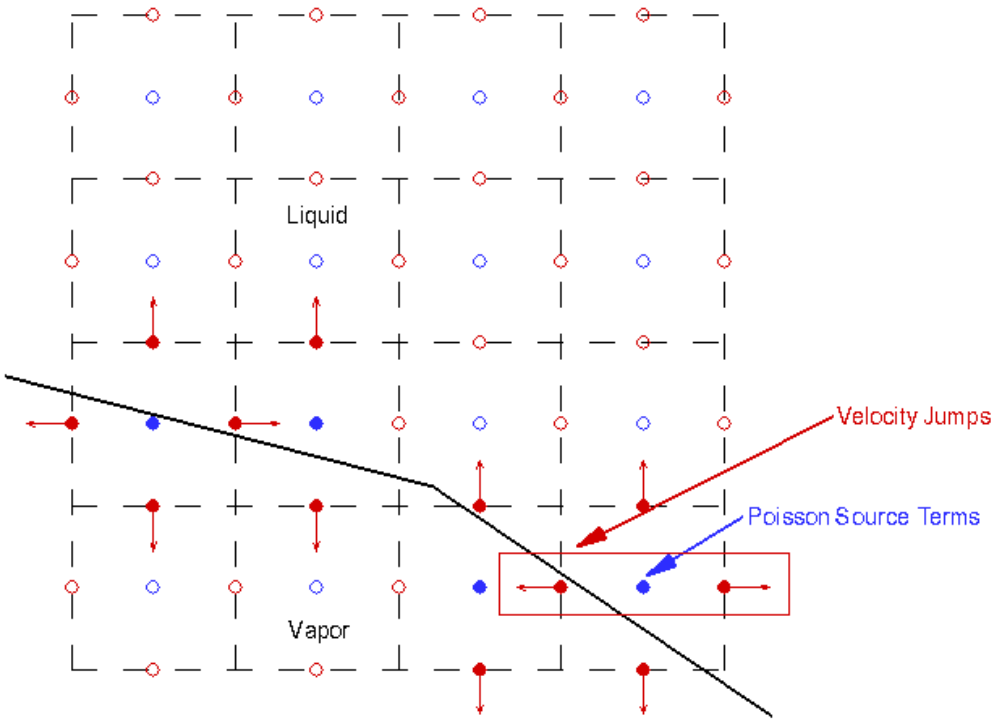

Figure 8: Discrete velocity jumps.

With this method, some cells containing an interface will not have a source term because the velocity points on opposite faces are not separated by the interface. This is illustrated in Figure 8 where the third cell from the left in the third row from the top contains an interface but no source term and no velocity jumps. Also, cells with an

interface that is not aligned with the grid may still only have a velocity jump in one direction, for example the second cell from the left in the third row from the top of Figure 8 has an interface with a normal component in the left-to-right direction, but no velocity jump in that direction.

The discrete velocity jump method produced good results for some simple cases, such as an expanding bubble on a concentric mesh. However, with slightly more complex cases, such as a bubble on a square mesh, some non-physical behavior could be seen as the interface moved from separating one pair of velocity points to separating another set and a source was suddenly added or removed from a cell when it shifted to a neighboring cell. Furthermore, this method caused instability when a bubble was in contact with a solid boundary and source terms would be added or removed without a neighboring cell loosing or gaining a source of similar magnitude.

The velocity jump is now treated in an integral fashion by considering the production of a flux jump by the phase change which results in a jump in the average velocity at cell faces. It is not necessary for the interface to separate two velocity points. The ratio of the area of the interface in a given direction to the mean area of the cell faces in that direction is used to modify the expected velocity jump.

$$[\boldsymbol{u}] = \dot{m}\left[\frac{1}{\rho}\right]\frac{A_i}{A_f}\,\boldsymbol{n} \tag{47}$$

where A_f is the face area and A_i is the interface area. The interface area is determined from the sharp VOF method by finding the points where the interface intersects the cell edges, as described by Wang *et al.* (2012). The area is then computed by a series of cross-products between the interface edge vectors.

With this method, source terms slowly increase and decrease in a cell as the interface moves through the cell. If a cell has a volume fraction between zero and one, then it will contain a volume source contributing a flux jump proportional to the interface area and normal component in each direction. These area ratios are used to modify the

coefficient in the Poisson equation. Figure 9 illustrates the application of this method. Compared with Figure 8, the flux jump method shows source terms included in more cells, and velocity jumps in any direction in which the interface normal has a component.

Ghost Fluid Method

In the ghost fluid method, separate liquid and vapor velocity fields are created by extending the liquid solution into the vapor region and by extending the vapor solution into the liquid region. This provides the required layers of ghost fluid cells on each side of the interface for use in the higher order stencils used in the momentum solver. Each field is then separately advanced in time through the momentum solver. The two fields are then combined based on the interface location.

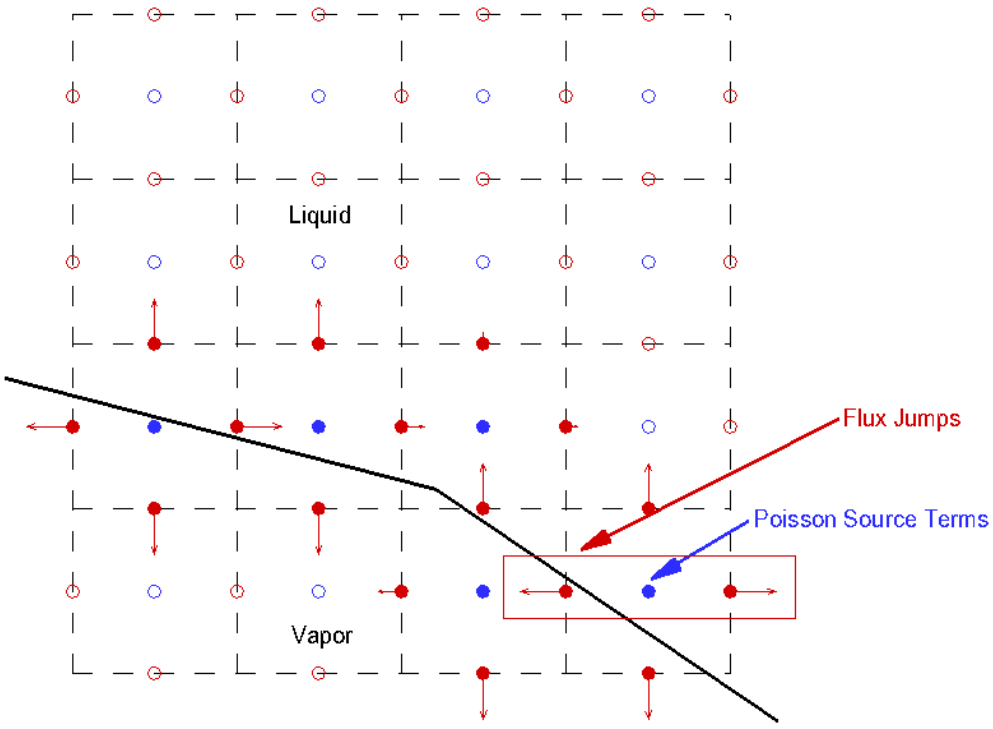

Figure 9: Flux jumps.

The ghost fluid method was introduced by Fedkiw *et al.* (1999a) for multiphase compressible flows without phase change and extended by Nguyen *et al.* (2001) to incompressible flame fronts with mass transfer. The method was employed by Son and Dhir (2007) and Gibou *et al.* (2007) using the level set method to compute boiling problems.

The momentum solver used in this research includes the effects of surface tension and the density and viscosity changes between the fluid fields (Yang and Stern, 2009). Therefore, the ghost fluid method is only applied to the normal velocity jump due to phase change.

To extend the liquid velocity field, the jump in normal velocity is removed from cells in the vapor region by applying

$$\boldsymbol{u}_l = \boldsymbol{u}_v - \dot{m}\left[\frac{1}{\rho}\right]\boldsymbol{n} \tag{48}$$

at cells where the volume fraction is equal to zero, therefore all vapor. The normal is available from the level set function. To determine the value of $\dot{m}$ away from the interface, the level set fast marching method developed by Yang and Stern (2011) has been modified to simultaneously extend the value of $\dot{m}$ at the interface in the normal direction, following the method described by Herrmann (2003)

A similar method is applied to extend the vapor velocity field into the liquid region.

$$\boldsymbol{u}_v = \boldsymbol{u}_l + \dot{m}\left[\frac{1}{\rho}\right]\boldsymbol{n} \tag{49}$$

The interface location at time *n* is used to extend and separate the velocity fields. The interface location is then advected to time *n+1* using the interface velocity and the new location of the interface is used to merge the velocity fields. The sign of the level set function is used to determine whether the liquid or vapor velocity is used for the

combined field. This method assures the correct location of the velocity jumps in the combined velocity field.

Pressure Boundary Condition

A fixed pressure boundary condition was added to support cavitation modeling. This type of boundary allows volume sources to drive fluid into or out of the domain. This type of boundary was very useful for the bubble cases. For the foil case, a mixed boundary condition was created to allow the outer boundary of an O-grid to have a specified inflow velocity upstream of the foil and a specified pressure downstream of the foil. Calculations for the foil were also performed with a convective outlet.

Cavitation Inception

A simple model is used to create bubbles where the pressure falls below a specified pressure for inception. An initial radius is also specified. The point of minimum pressure in the flow field is located and the local grid size is determined. The code checks that the bubble radius is at least 2.5 times the local grid size to be sure that the grid is adequate to represent the bubble before creating it.

A bubble is created by computing the level set function for the new bubble and comparing it will the existing level set values at cell centers. The lowest value is then used. The volume of fluid scalar is initialized using a subdivision of the cells at the interface to compute the approximate vapor fraction following Wang *et al.* (2012).

This method is relatively crude. Even with a fine grid, the initiation of a bubble creates a strong disturbance in the pressure field. In the future, it would be best if the sharp interface cavitation model could be coupled to a subgrid model, such as the mixture model, to ease the initial bubble creation and final destruction.

VERIFICATION AND VALIDATION

Two-Dimensional Vapor Bubbles

Two-Dimensional Vapor Bubble on a Circular Mesh

The first validation case is the simple two-dimensional case of an expanding vapor bubble on a circular mesh. The initial radius of the bubble is one. The O-grid is 128×128 cells, with a radius of 10 and points clustered near the interface, as shown in Figure 10. The phase change rate is specified so that the total volume source will be constant.

$$\dot{m} = \frac{0.1}{r}\left(\frac{1}{\rho_v} - \frac{1}{\rho_l}\right) \tag{50}$$

where *r* is the local radius. This creates a pressure and velocity field outside of the bubble which is the same as the field created by a source of constant strength at the center of the mesh. Inside of the bubble, there is no flow and the pressure is constant.

Figure 12 shows the radial distribution of pressure. The analytical solution for a source of constant strength at the center of the mesh is shown in black. The colored curves show the solution over 50 time steps. As the bubble expands, the radius increases and the pressure inside the bubble rises to match the pressure at the new interface radius, as illustrated in the figure.

Two-Dimensional Vapor Bubble on a Square Mesh

The second case is the same expanding vapor bubble on a square mesh. The Cartesian grid is 512×512 cells, with dimensions of -10 to 10 in both directions. The mesh is finer in way of the bubble, as shown in Figure 11.

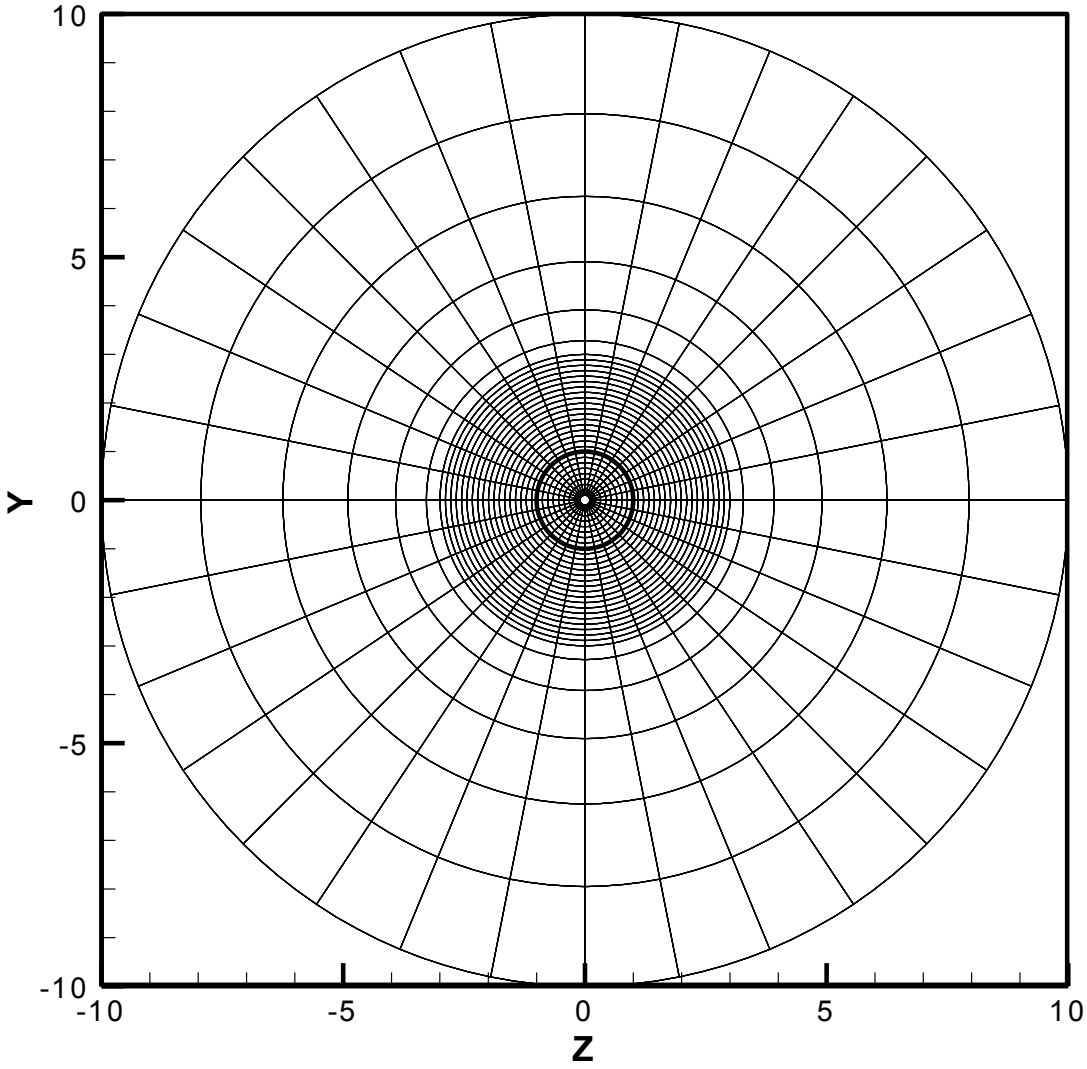

Figure 10: Round mesh (for clarity, every fourth grid line is shown).

Figure 13 shows the radial distribution of pressure on the square mesh. The analytical solution for a source of constant strength at the center of the mesh is shown in black. The colored curves show the solution over 50 time steps and all solution points within a radius of 10. As the bubble expands, the radius increases, the pressure inside the bubble rises to match the pressure at the new interfacial radius, as illustrated in the figure. Comparison with the circular mesh results in Figure 12 shows that the square mesh

introduces some discretization errors. The use the flux jump method has greatly reduced these errors compared to the discrete velocity jumps used previously.

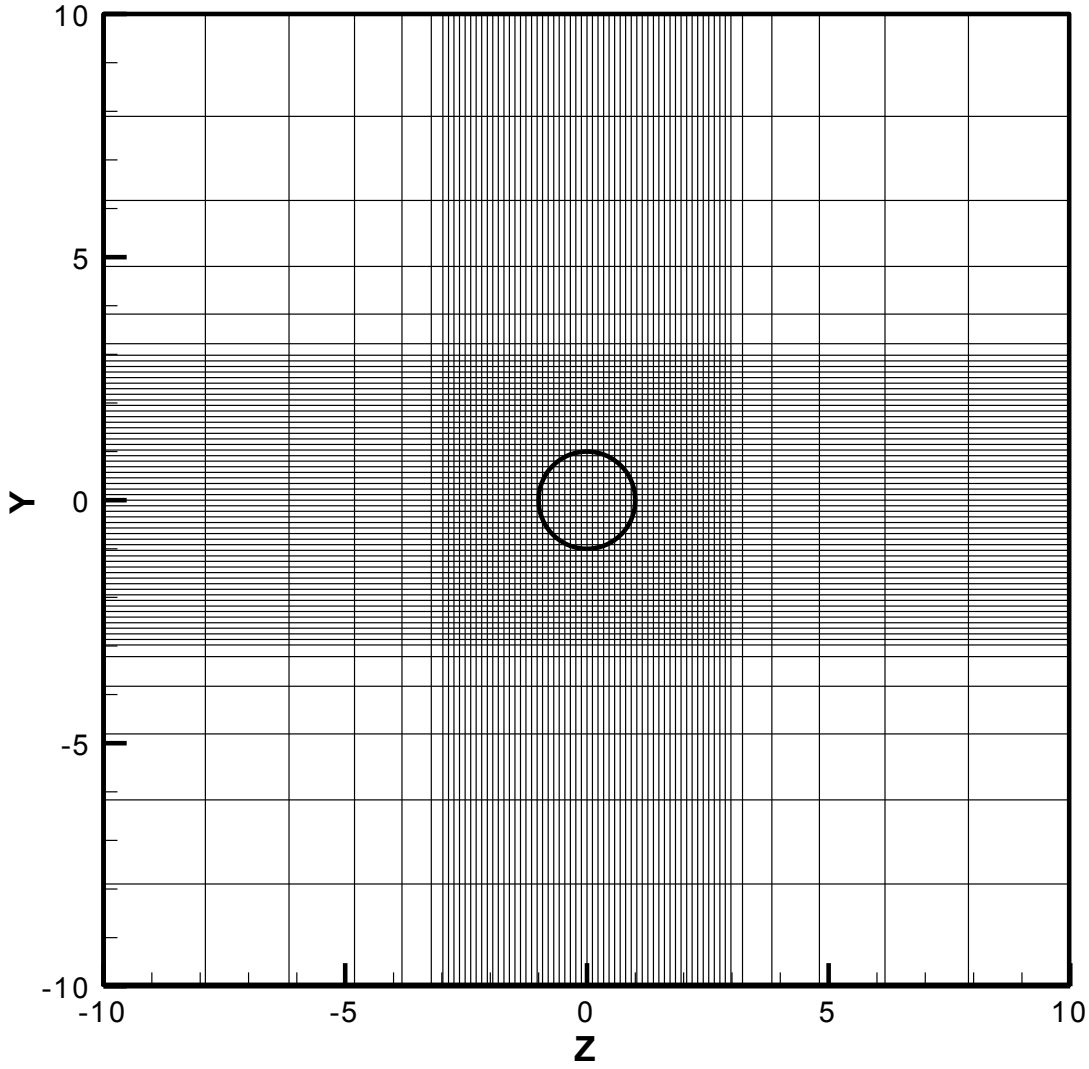

Figure 11: Square mesh (for clarity, every eighth grid line is shown).

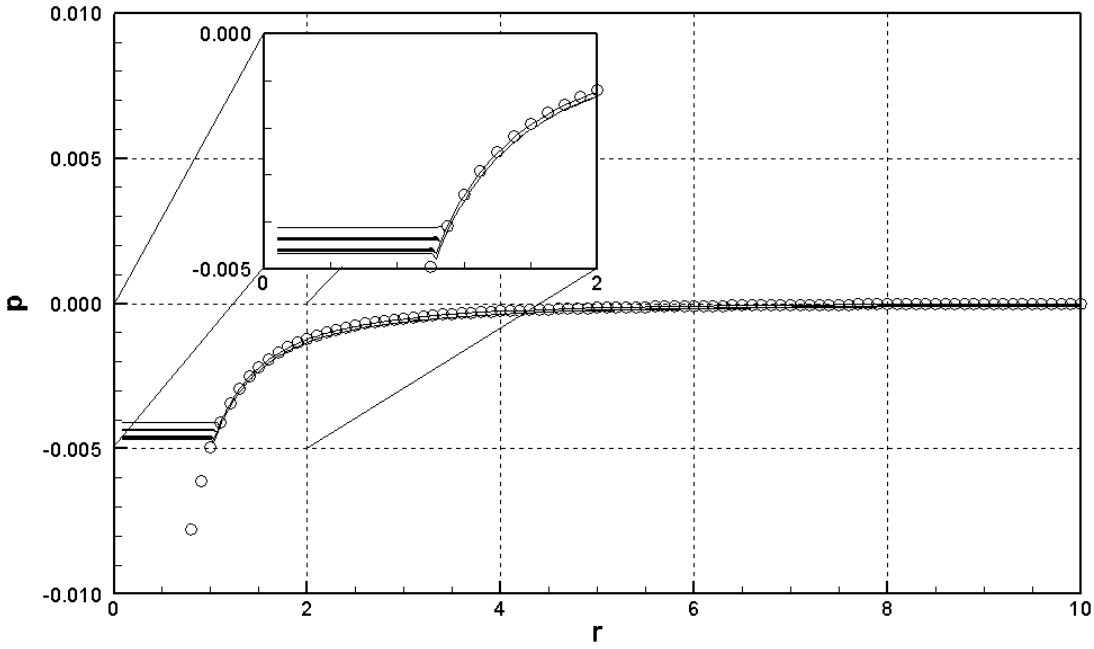

Figure 12: Radial pressure distribution of expanding bubble on a circular mesh.

Two-Dimensional Vapor Bubble on a Square Mesh with Computed Phase Change Rate

The semi-implict phase change rate model was applied to the bubble on the square mesh. The boundary pressure was specified as zero, while the vapor pressure was set to a positive value, in this case two. Because the boundary pressure is below vapor pressure, the bubble will expand indefinitely in this contrived case.

Figure 14 shows the radial pressure distribution for 30 time steps. Initially, the pressure inside the bubble rises to a point close to vapor pressure. This is necessary to accelerate the fluid surrounding the bubble so that the bubble can begin to grow. As time passes the velocity around the bubble increases and the pressure surrounding the bubble falls due to the higher velocity than the boundary. The pressure inside the bubble is also reduced while it continues to expand.

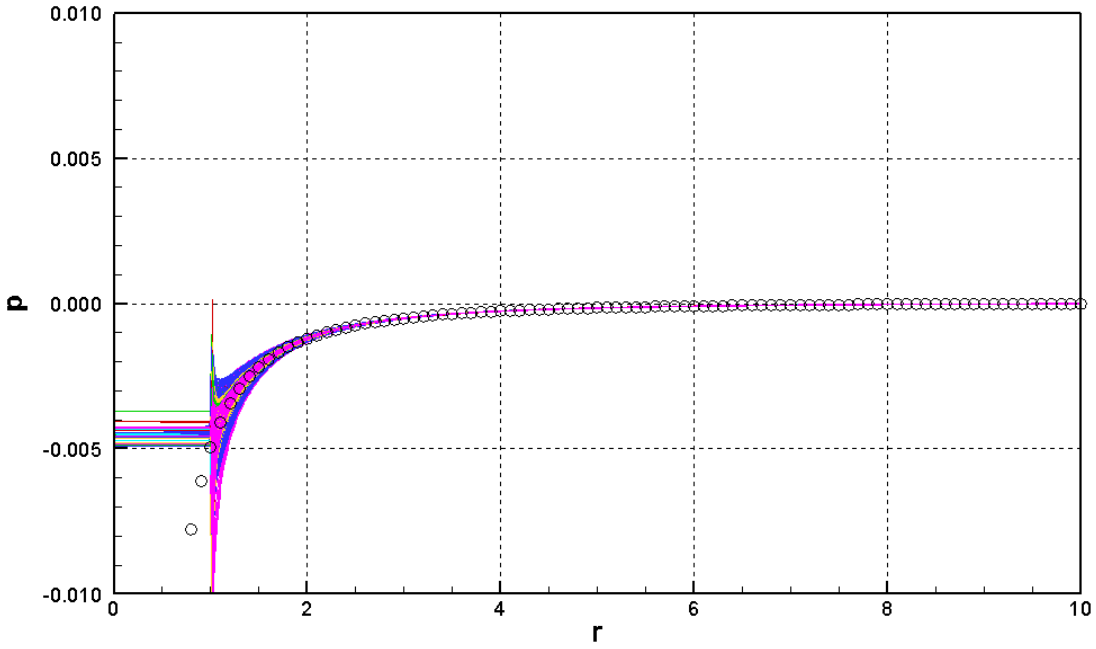

Figure 13: Radial pressure distribution of expanding bubble on a square mesh.

As in Figure 13, all solution points inside of a radius of 10 are shown in Figure 14. The errors near the interface shown in Figure 13 are not present here because of the coupling between the pressure and the phase change rate.

Figure 15 shows the velocity and pressure solution near the upper left of the bubble after 50 time steps. The jump in velocity is clearly visible. Some pressure variation occurs along the interface due to discretization.

As the bubble grows, the Rayleigh-Taylor instability, which affects less dense fluids expanding into more dense fluids, causes waves to develop at the interface. "Fingers" of liquid push into the vapor bubble. As these fingers release droplets, the solution becomes unstable. It is believed that this is a problem with the implementation of the ghost fluid method. When a droplet contains a single cell center, the velocity jump applied at that lone point is determined by the closest interface and the normal there. The velocity is not representative of the drop as a whole. Movement of the interface will

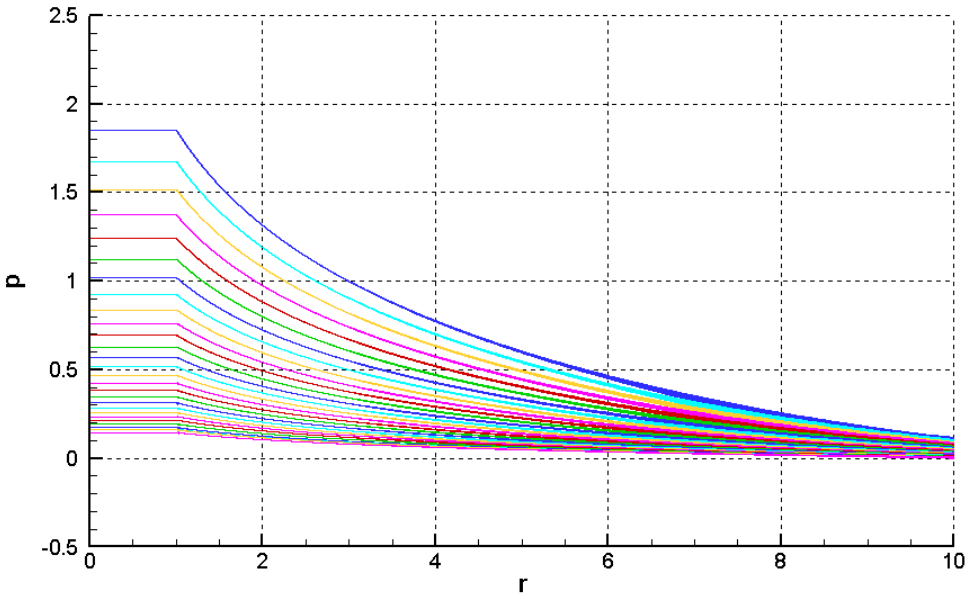

Figure 14: Pressure distribution with semi-implicit model.

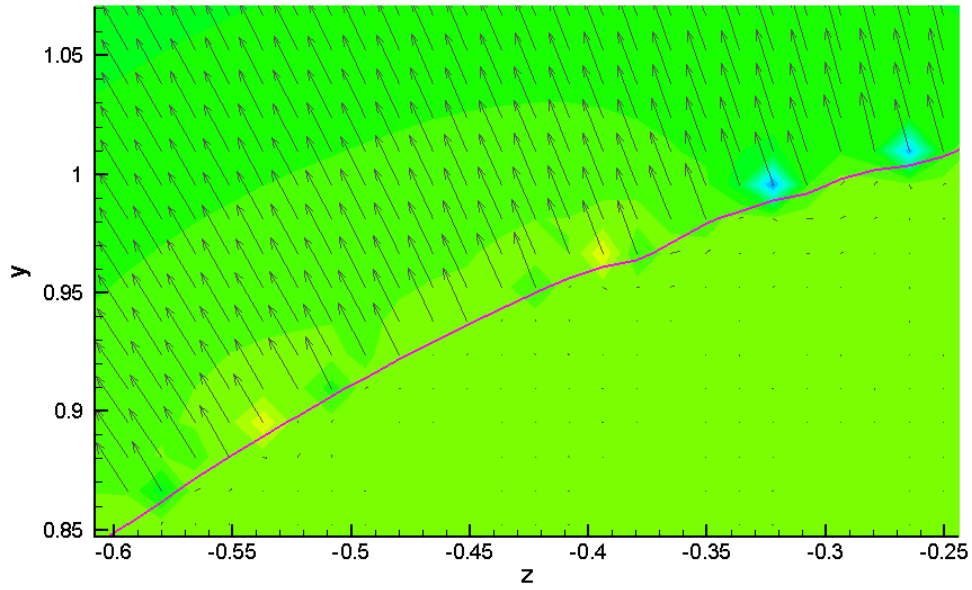

Figure 15: Velocity and pressure at the interface.

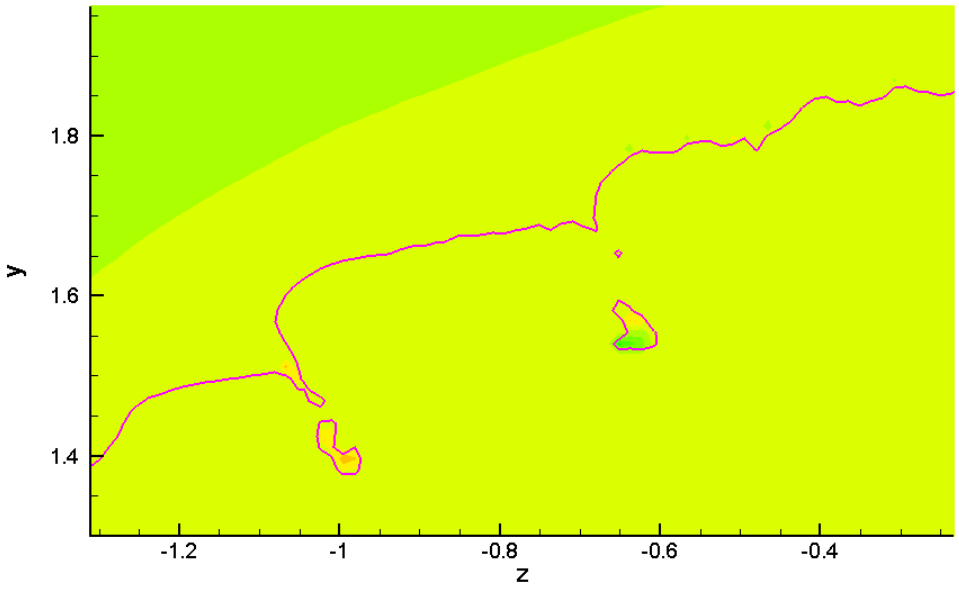

Figure 16: Interface shape after 178 time steps.

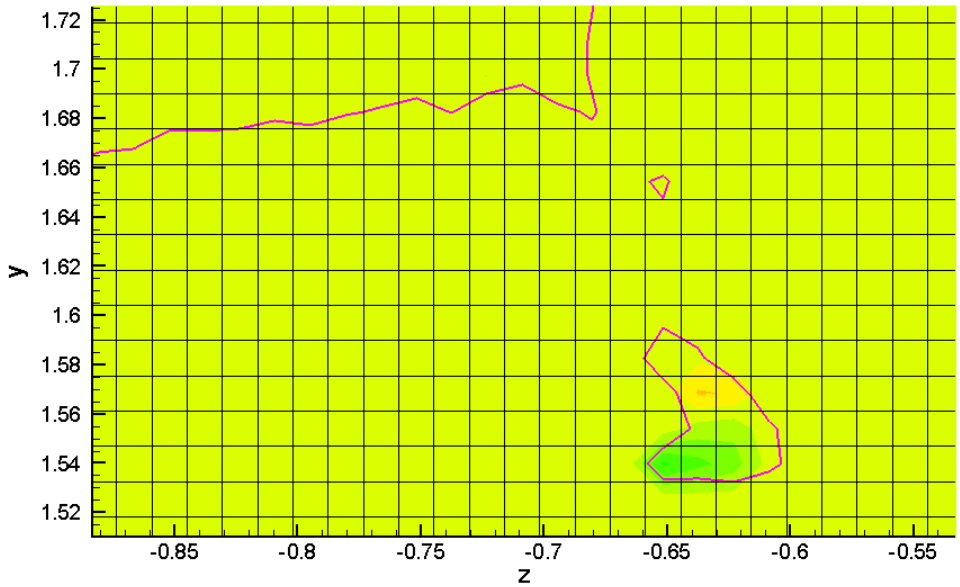

Figure 17: Small droplets with grid.

change the closest point so that non-physical velocities may be applied to the lone cell center contained by the droplet. This can be severe enough to cause the solution to diverge. Figure 16 illustrates the shape of the interface in the upper left portion of the bubble. Note the tiny droplet to the left of the center of the figure and the non-physical pressure solution in the small droplet below it. Figure 17 shows a closer view of this area and the computational cell faces.

Figure 18 shows a closer view of the small drop, which is defined by the contour where level set is zero. The figure also shows the volume fraction of liquid at each cell center point. It is clear that some differences between the volume of fluid method and the level set method can arise when drops become this small.

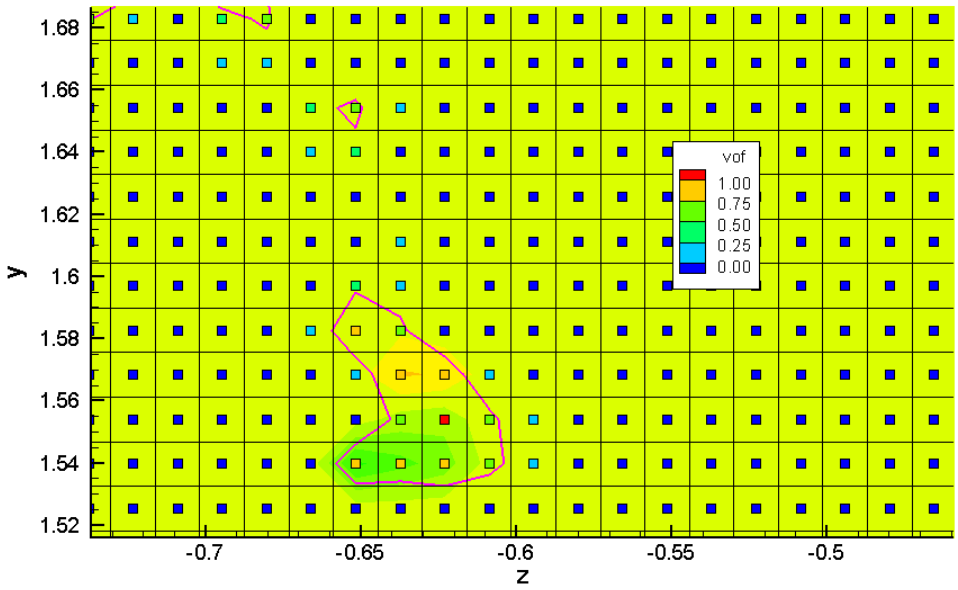

Figure 18: Small droplet and liquid volume fraction.

Methods of identifying and applying special handling to small droplets are being investigated. It is likely that a similar problem exists for bubbles occupying only one cell. The sharp interface methods are not well suited to bubbles of this size. Ideally, the

sharp interface method would be coupled with a discrete bubble model and bubbles would be exchanged between models as the bubbles crossed size limits determined by the local grid size. However, that is beyond the scope of this work.

Half of a Two-Dimensional Vapor Bubble on a Square Mesh

To compute surface cavitation on hydrofoils, the method must be robust on a solid boundary. This has been tested through the use of a case similar to the bubble on a square mesh, but with half of the mesh removed and replaced by a solid boundary. It was found that the method remains stable and produces similar results to the complete bubble described above. The level set function is extrapolated at the boundary.

Half of a Two-Dimensional Vapor Bubble on a Square Mesh with Cross Flow

To further prepare for the foil calculation, a half-bubble on a solid boundary was computed in the presence of cross flows of varying strength. The cross flow causes a significant deformation of the bubble, as expected. The method remains stable until small droplets are formed. Figure 19 shows the bubble in a cross flow of u=0.5 at 90 time steps after inception. The small black circle near (0,0) indicates the approximate bubble size and location at inception.

The figure shows that the bubble has moved downstream while growing and that the flow has been forced around the growing bubble, as expected. The growing bubble produces a wake, similar to a point source in potential flow. The base of the bubble on the upstream side is disturbed by the stagnation point that forms there.

This calculation is the most similar to the case of a cavitation bubble on a hydrofoil. Missing is the curved shape of the surface and the resulting pressure field with an adverse pressure gradient downstream.

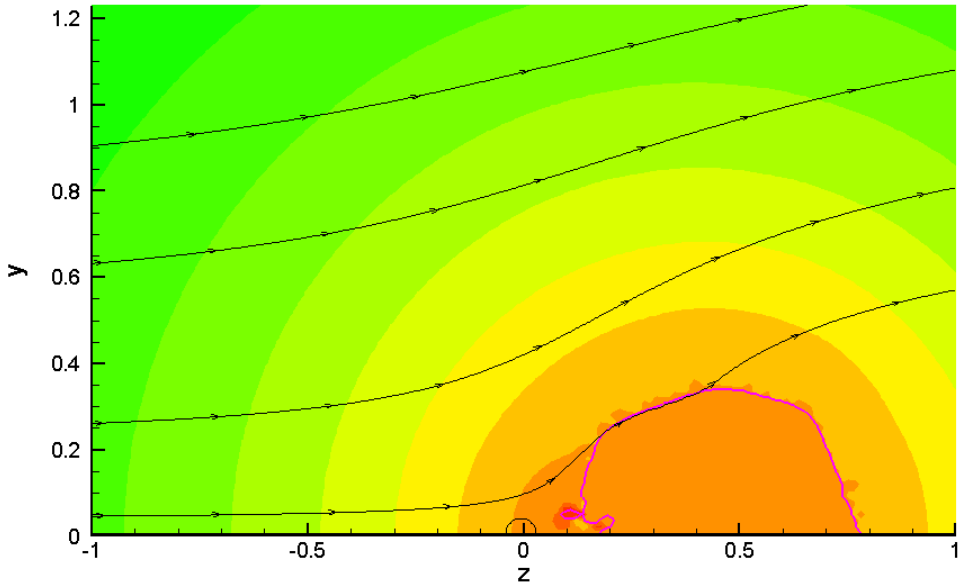

Figure 19: Bubble in cross flow.

NACA 66 Hydrofoil at Six Degree Angle of Attack

A hydrofoil with a NACA 66 thickness distribution, a thickness-to-chord ratio of 0.09, a NACA a=0.8 meanline, and a camber-to-chord ratio of 0.02 was tested by Shen and Dimotakis (1989a,b). Figure 20 depicts the hydrofoil. The lift and pressure distribution on the foil were measured for a variety of conditions with and without cavitation. Here, the case with a six degree angle of attack and an inflow has been modeled. The Reynolds number based on chord length is 2×10^6.

Non-Cavitating Solutions

To evaluate grid dependence, three grids of increasing resolution were used to compute pressure distributions and lift coefficients for comparison with the experiment. The fine grid was generated first. Then, the medium grid was created by discarding even numbered points from the fine grid. Finally, the coarse grid was created by discarding the even numbered points from the medium grid.

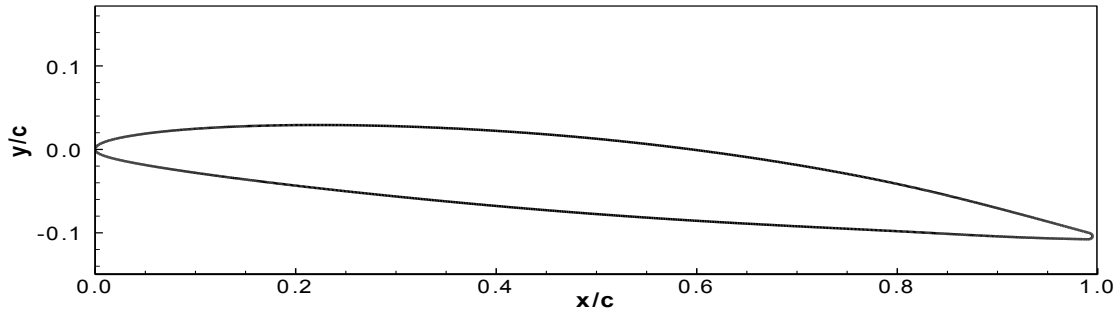

Figure 20: Geometry of Hydrofoil.

A slip boundary condition was used on the foil to avoid separation which would occur due to the lack of a turbulence model and the large height in wall units, of the first cell. The lift of hydrofoils at high Reynolds number is generally well predicted by potential flow codes because the viscous effects are relatively unimportant to the lift. Therefore, the use of a slip boundary rather than a no-slip boundary is acceptable, although not ideal.

Table 1 lists the dimensions of the grids, the height of the first cell from the wall in wall units, and the computed lift coefficients. The experimentally measured lift coefficient for this condition was 0.786. All three grids have a radius of approximately ten chord lengths. The medium grid at the leading edge of the foil is shown in Figure 21.

Figure 22 compares the chordwise pressure distribution on both sides of the foil with the experimentally measured values. Note that, following tradition, $-C_P$ is shown so that the pressure distribution on the "upper" surface of the foil in Figure 20 is shown on top in Figure 22. The pressures agree reasonably well, which will be important for the cavitating calculation.

Cavitating Parametric Studies

The fine grid described in the non-cavitating solutions section was used for the majority of the cavitating solutions. The current, crude inception model was used to

generate a few bubbles near the leading edge. Inception was then disabled and the cavity was allowed to evolve from these initial bubbles. The initial bubbles quickly merge and begin to grow, mostly downstream.

Table 1: Hydrofoil grids and lift coefficients.

	Coarse	Medium	Fine
Dimensions	64×512	128×1024	256×2048
y+ at foil surface	200	100	50
Lift Coefficient	0.865	0.854	0.824
Error	10.1%	8.6%	3.3%

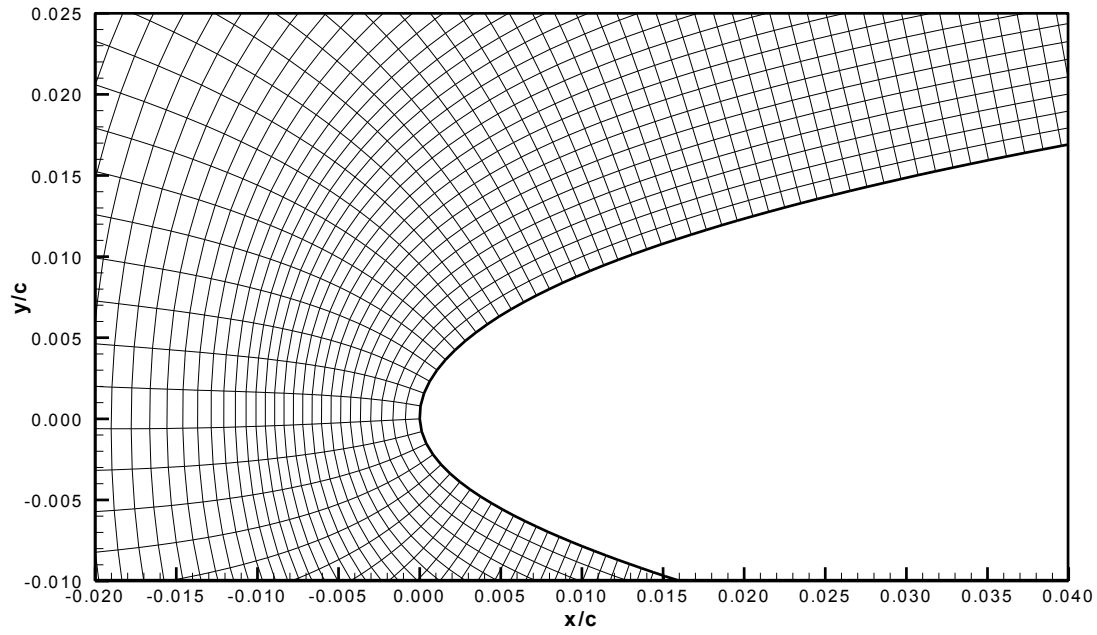

Figure 21: Medium grid at leading edge of hydrofoil.

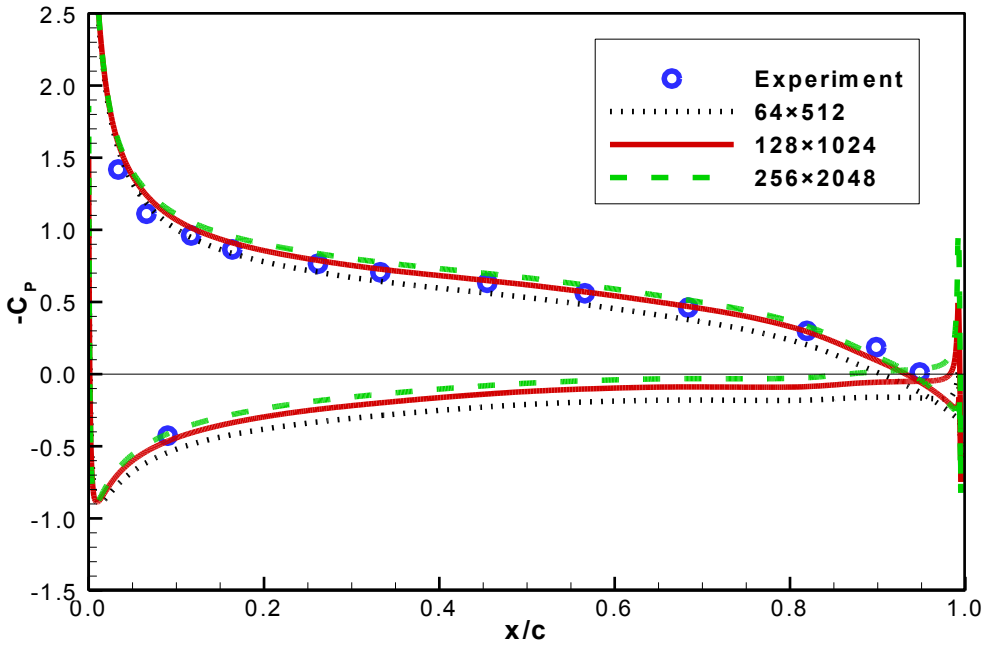

Figure 22: Comparison of computed and measured surface pressures.

It was found that the use of a no-slip condition on the foil surface was critical to keep the bubbles from quickly travelling downstream. This is at odds with the slip condition used for the non-cavitating solution. However, the no-slip condition is necessary to reproduce the physics of the cavitation bubble.

A parametric study of the effect of the vapor pressure and constants for evaporation and condensation was made to evaluate the effects of these parameters. Additionally, the importance of the vapor viscosity was also evaluated. Table 2 lists the fluid properties matching the experimental Reynolds number of 2×10^6, velocity of 12 m/s, and chord length of 0.1524 m (Shen and Dimotakis, 1989a). A temperature of 23.3ºC (74.0ºF) was determined based on the liquid kinematic viscosity required to match the Reynolds number of the experiment. The remaining properties were determined by the temperature.

Table 2: Fluid properties for hydrofoil calculations.

Liquid Density	997.4 kg/m^3
Vapor Density	0.02099 kg/m^3
Liquid Dynamic Viscosity	9.250×10^{-4} Pa s
Vapor Dynamic Viscosity	9.820×10^{-6} Pa s
Surface Tension	0.072 N/m

The cavitation number is defined as the difference between the far field pressure and the vapor pressure normalized by the free stream dynamic pressure:

$$\sigma = \frac{p_\infty - p_v}{\frac{1}{2}\rho U^2} \tag{51}$$

Cavitation numbers of 0.80 to 1.00 were investigated. Figure 22 shows that the lowest pressure coefficient on the wetted foil surface is below 2.5 with a far field pressure of zero, so cavitation is expected near the leading edge.

Figure 23 compares the cavities at cavitation numbers of 1.0, 0.9, and 0.8 at the same time step. When the cavitation number is reduced, the vapor pressure is lower and the cavity grows larger. When a bubble is shed downstream, during the time it takes for the bubble to disappear, the pressure at the interface is maintained at vapor pressure. For this comparison, an evaporation coefficient of 3.5 and a condensation coefficient of 1.0 were used.

Figure 24 shows the evolution of the cavitation on the foil with a cavitation number of 1.0. The first time step corresponds to the time step shown in Figure 23. Bubbles are shed downstream from the cavity in a repeating cycle.

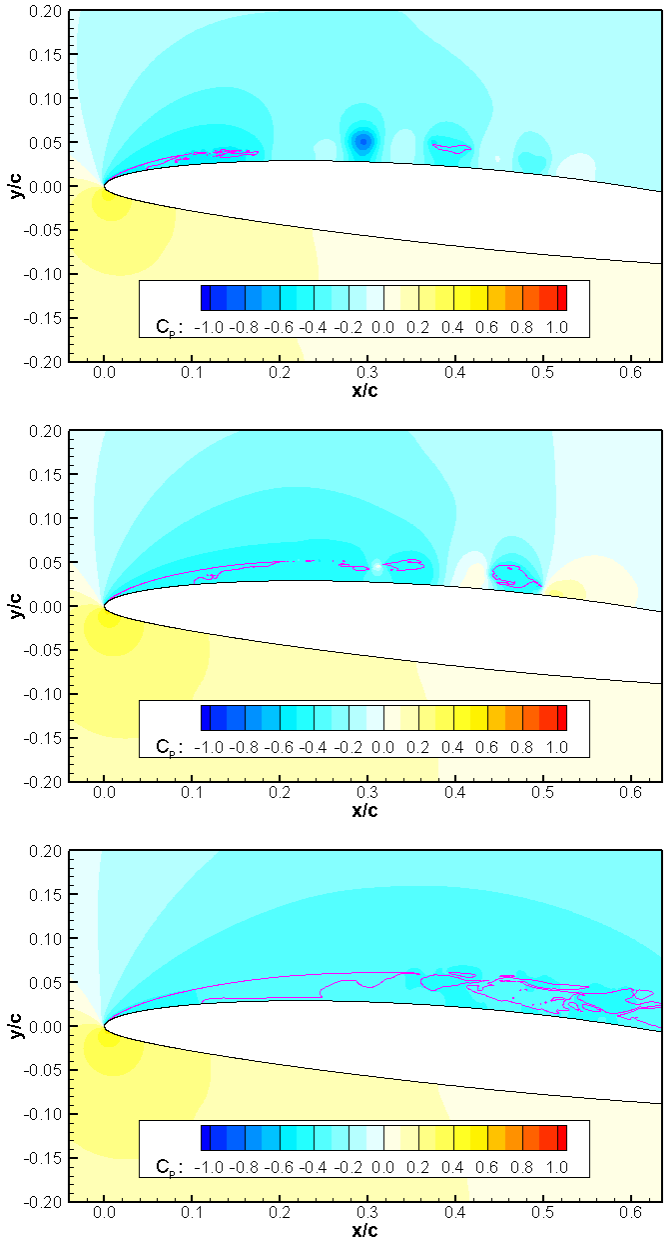

Figure 23: Comparison of cavitation numbers of 1.0, 0.9, and 0.8 from top to bottom.

The rate of evaporation is important for establishing and maintaining the position of the leading edge of the cavity, where the rate of evaporation must balance advection. If the rate of evaporation is insufficient, the cavity will travel downstream despite the low pressure at the leading edge. In that case, the inception of new cavities would create unsteady cavitation at the leading edge. Evaporation coefficients of three to four were found to produce a stable cavity leading edge position.

The rate of condensation determines the how long the cavity, or shed cavities, persist downstream. This is significant because the existence of any cavity has a strong effect on the local pressure field by forcing the pressure at the interface to be close to vapor pressure. As determined by Singhal *et al.* (2002), a lower rate of condensation than evaporation produced better results. When the rate of condensation is equal to the rate of evaporation, the cavity is very small. Figure 25 shows solutions at the same time step with condensation coefficients of 0.1, 1.0, and 2.0 at a cavitation number of 1.0.

The effect of vapor viscosity was also investigated and found to have some effect on the shedding of the cavities. Figure 26 shows solutions with vapor viscosities that are one-tenth and one-hundredth of the liquid dynamic viscosity. Both solutions are at the same time step with the same cavitation number, 1.0. As shown in Table 1, the ratio of liquid to vapor dynamic viscosity at room temperature is about one hundred.

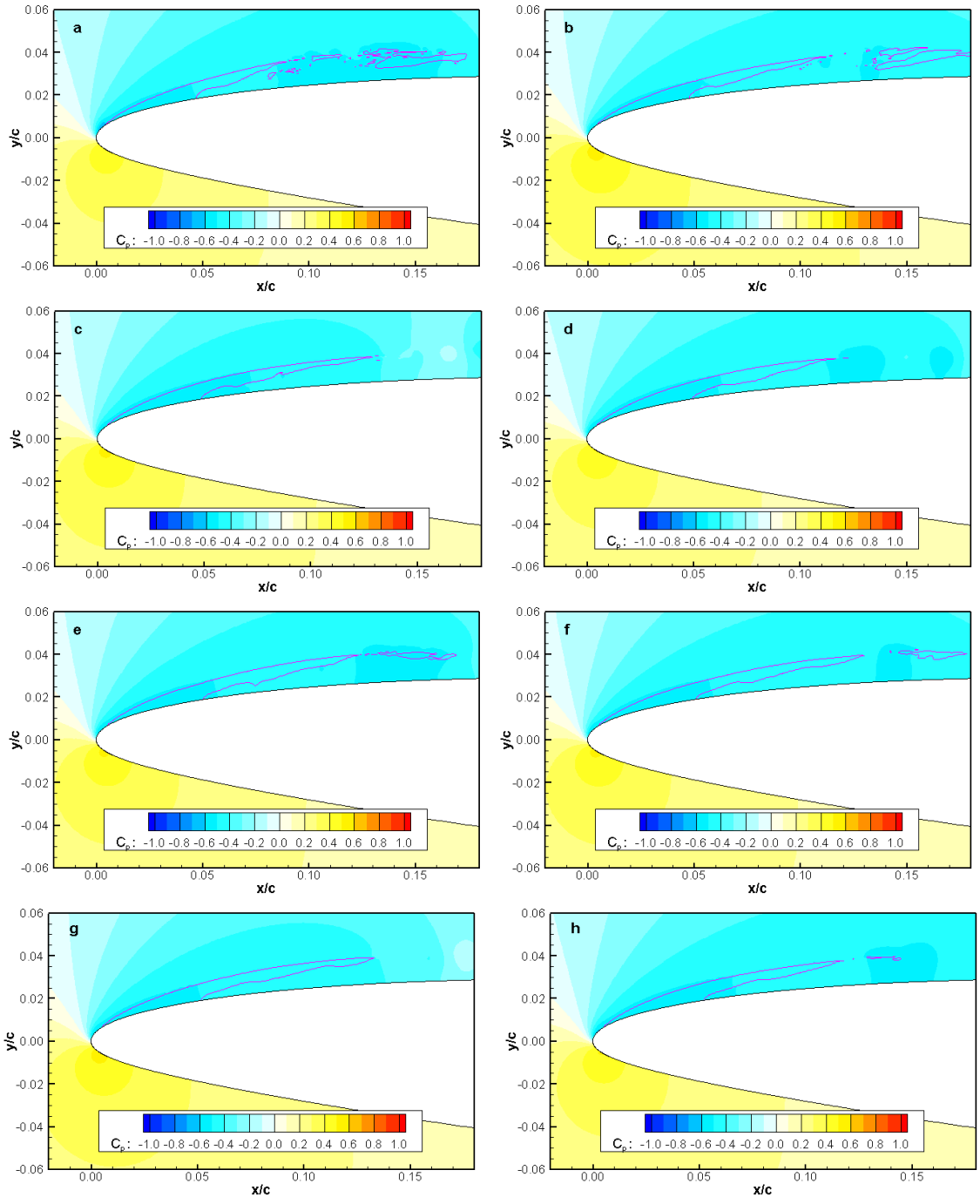

Figure 24: Leading edge cavity evolution.

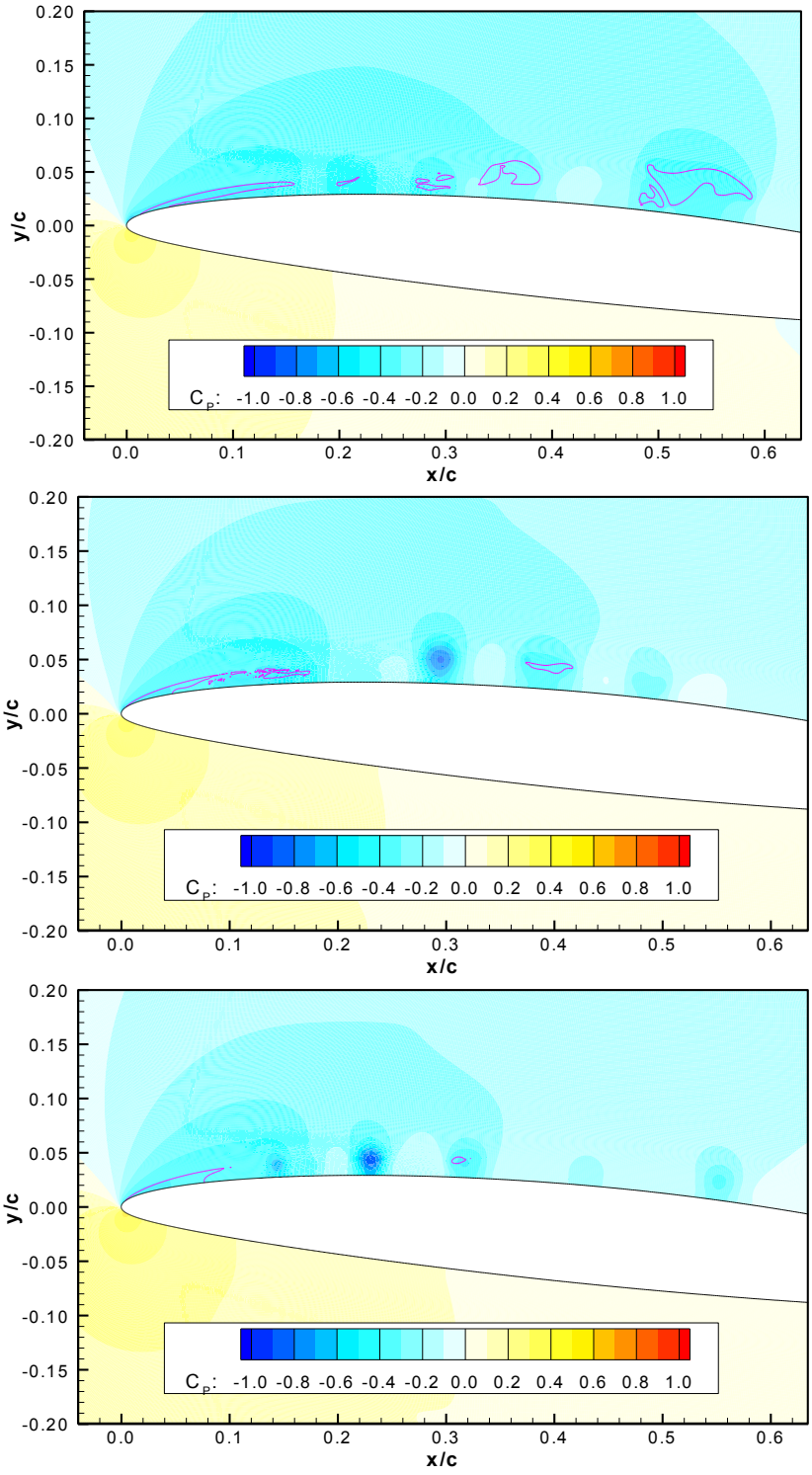

Figure 25: Condensation coefficients of 0.1, 1.0, and 2.0 (top to bottom).

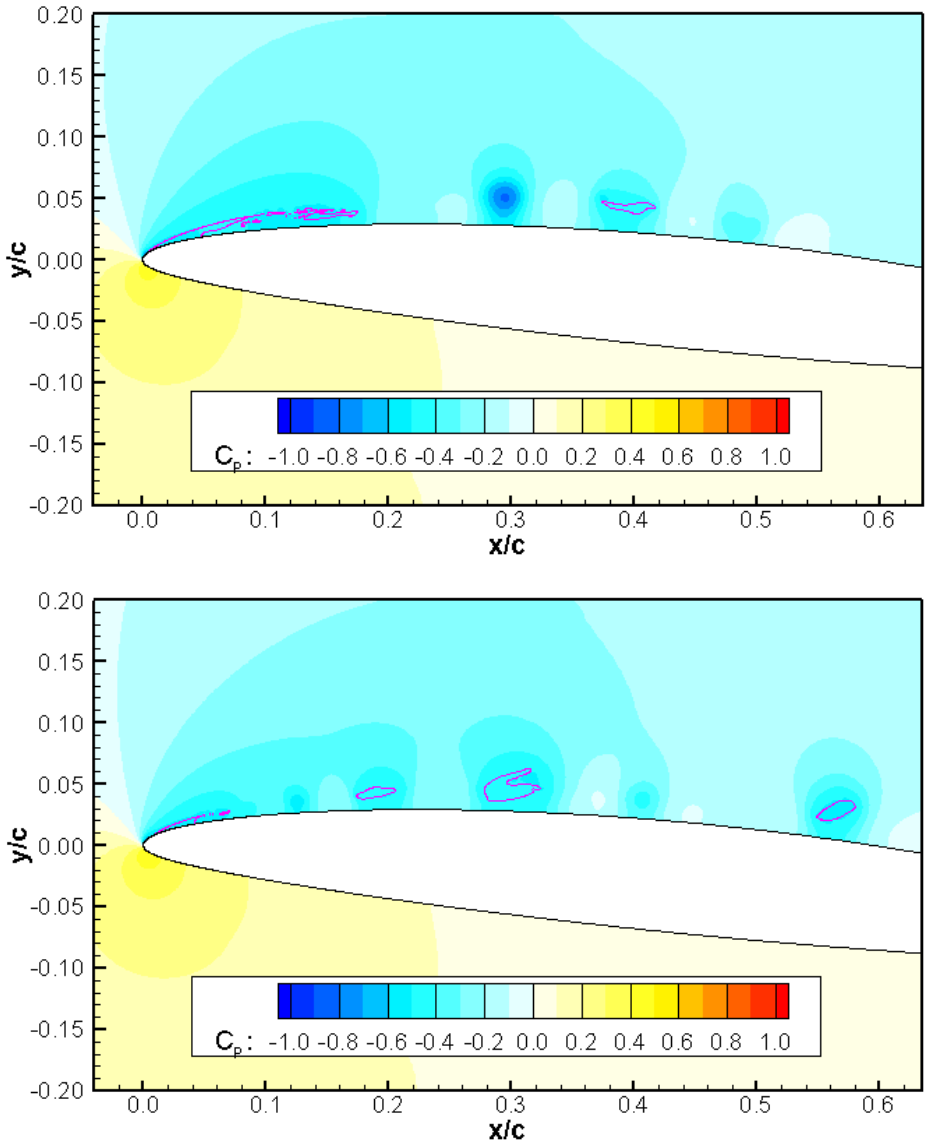

Figure 26: Vapor viscosities of one-tenth and one-hundredth liquid dynamic viscosity (top to bottom).

Comparison with Cavitating Experiment and Discussion of Shedding

Cavitating calculations were made for direct comparison with the experimental measurements. Figure 27 shows a view of the suction side of the hydrofoil at a six degree angle of attack with a Reynolds number of 2×10^6 and cavitation number of 1.22 (Shen and Dimotakis, 1989b), similar to the cavitation number of 1.25 for which pressure data was reported (Shen and Dimotakis, 1989a). Flow is from left to right.

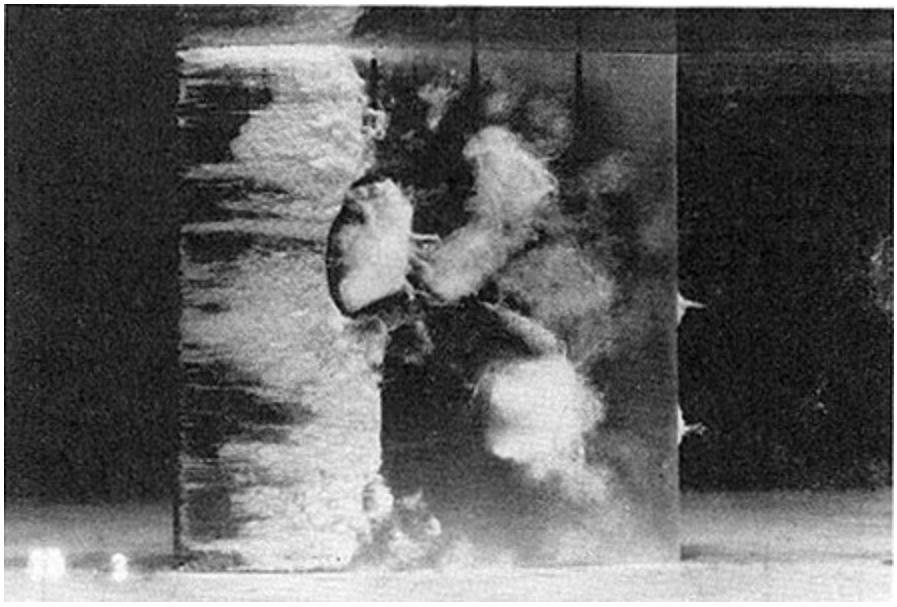

Figure 27: Cavitation on NACA 66 hydrofoil (Shen and Dimotakis, 1989b)

Figure 27 shows unsteady shedding occurring. A cavity is being shed approximately one-third of the span from the top of the photograph. Approximately two-thirds of the span from the top of the photograph, a shed cavity can be seen travelling downstream. The authors state that the cavity extends to about 40 percent of the chord, on average, varying between 35 and 45 percent of the chord. The pressure measurements are time averaged.

A computation at conditions matching the pressure measurements shows encouraging results. Although a long time average was not possible, the cavity develops to the proper size and the instantaneous pressure distribution matches the experimental measurements. Unfortunately, a problem in the solution of the Poisson equation prevents the calculation from continuing. It is believed that the large number of small bubbles and droplets that occur during the shedding results in a number of under-resolved bubbles or droplets. When a bubble or droplet is under-resolved, it may not be possible to determine an appropriate normal vector. Or, closely spaced volume sources of opposite sign may lead to trouble.

Figure 28 compares the computed pressure distribution with the experimental measurements. A stagnation point at the aft end of the cavity is clearly visible. This point is expected at the cavity closure and agrees with the findings of other researchers. It is believed that this stagnation point forces liquid backwards, underneath the cavity. It is this "reentrant jet" that creates the instability that causes shedding.

Figure 29 shows a time series of cavity development. The reentrant jet develops under the cavity at the same time the cavity grows downstream. Figure 30 is the next step in the time series and shows the location of the magnified figures that follow. Figures 31-35 show magnified views of parts of Figure 30 which display certain physics of interest. The vectors in all figures use the same scale.

Figure 31 shows the stagnation point at the trailing edge of the cavity. The velocity vectors clearly show the nature of the reentrant jet. Near the interface, the vapor moves tangent to the liquid and with similar speed. Within this part of the cavity, a shear layer is formed by the opposite velocities on the upper and lower surfaces. At the closure point, the vapor velocity is near zero. Also at the closure, the pressure is slightly above vapor pressure—some vapor is being converted to liquid in this region.

Figure 32 shows the forward end of the reentrant jet, where it has pushed furthest underneath the cavity. A small velocity toward the forward end of the hydrofoil is

visible. Also, some vapor bubbles are trapped in the liquid near the surface. The pressure under the cavity is close to vapor pressure, because the potential for phase change at the interface acts quickly to maintain the pressure near vapor pressure, as described by Equation (28).

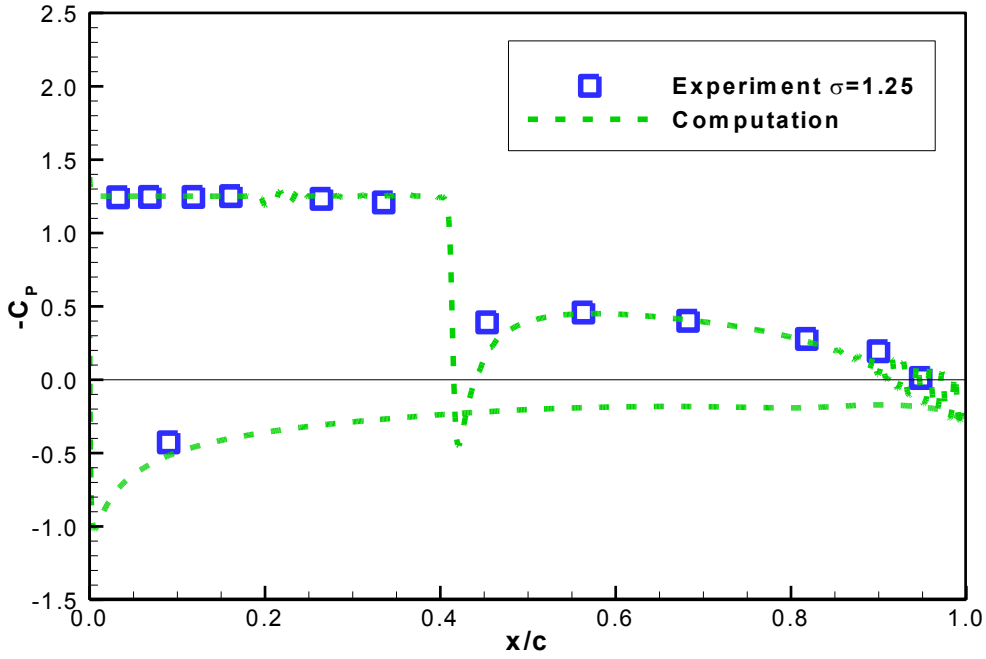

Figure 28: Comparison of measured and computed pressure distributions.

Figure 33 shows the complexity of the cavity flow in the region where the shedding process has begun. A number of liquid droplets appear in the vapor cavity. Collision of the droplets with the outer surface of the cavity causes bumps to appear, as shown in Figure 34. The bumps destabilize the interface. Eventually, the reentrant jet and the outer surface of the cavity will connect and a portion of the cavity will be shed downstream.

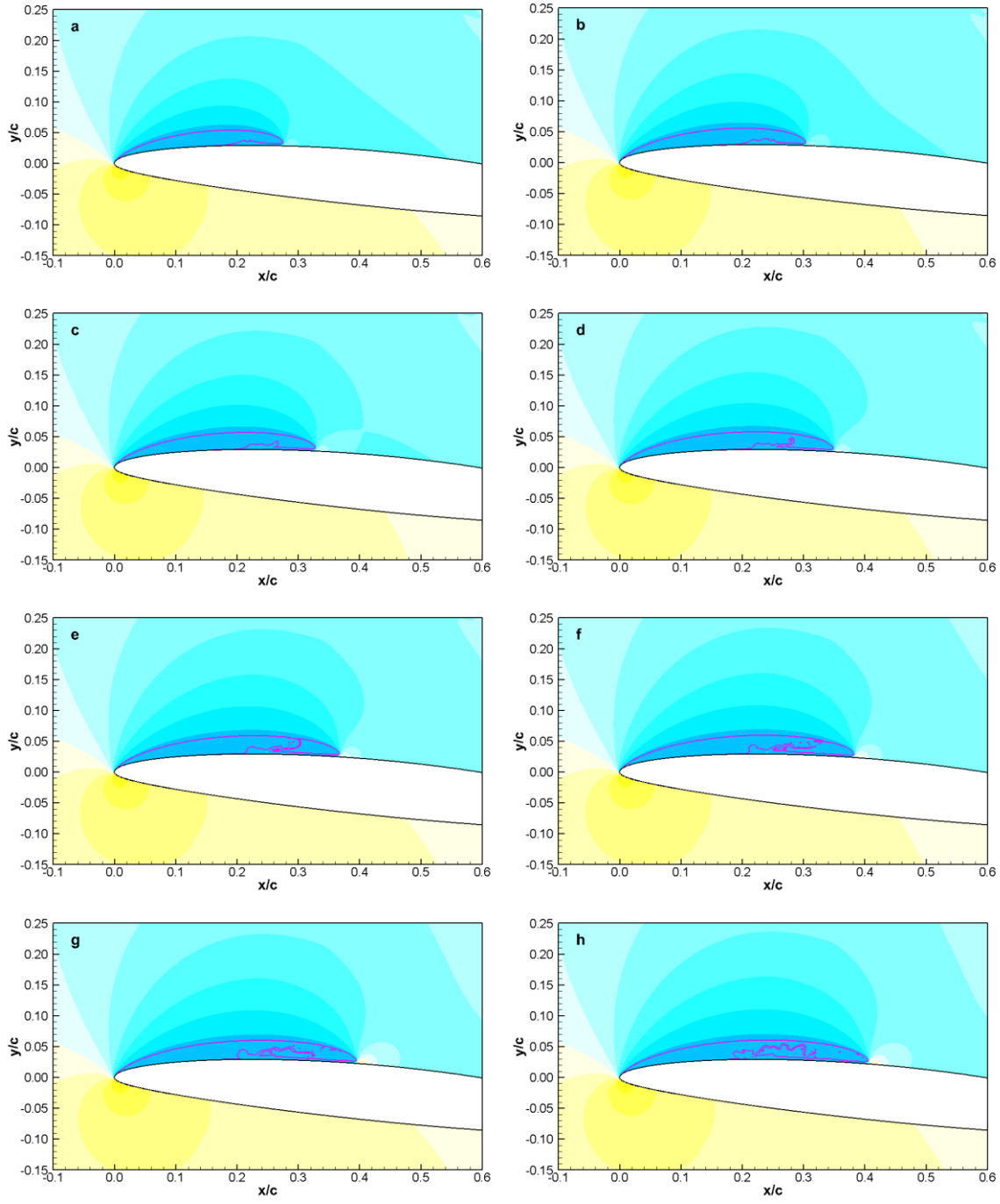

Figure 29: Time series of cavity development.

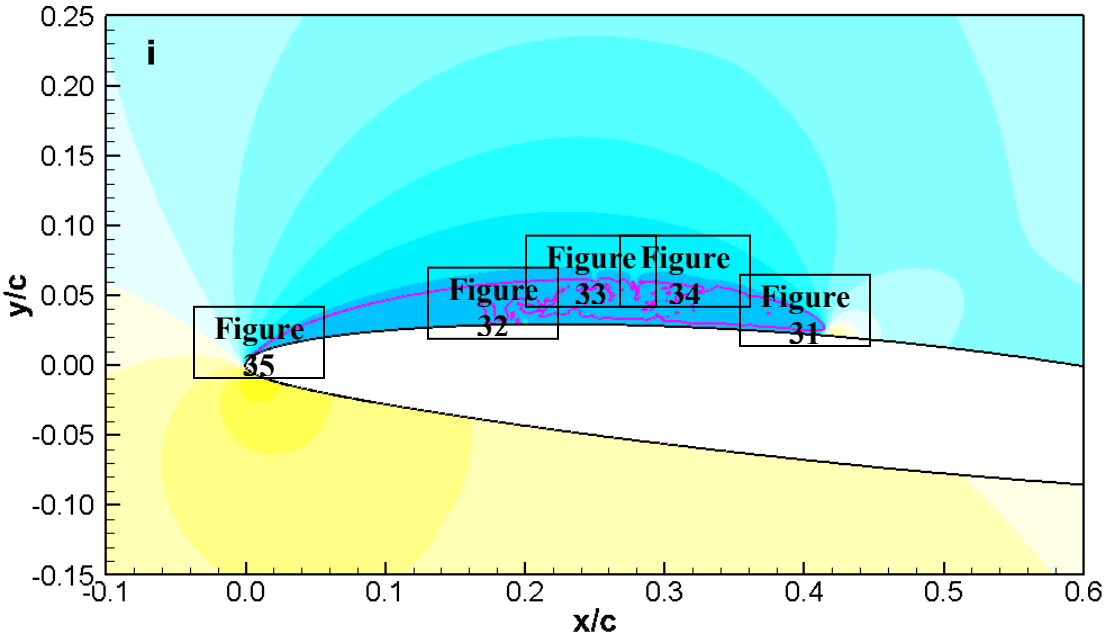

Figure 30: Cavity nearing shedding.

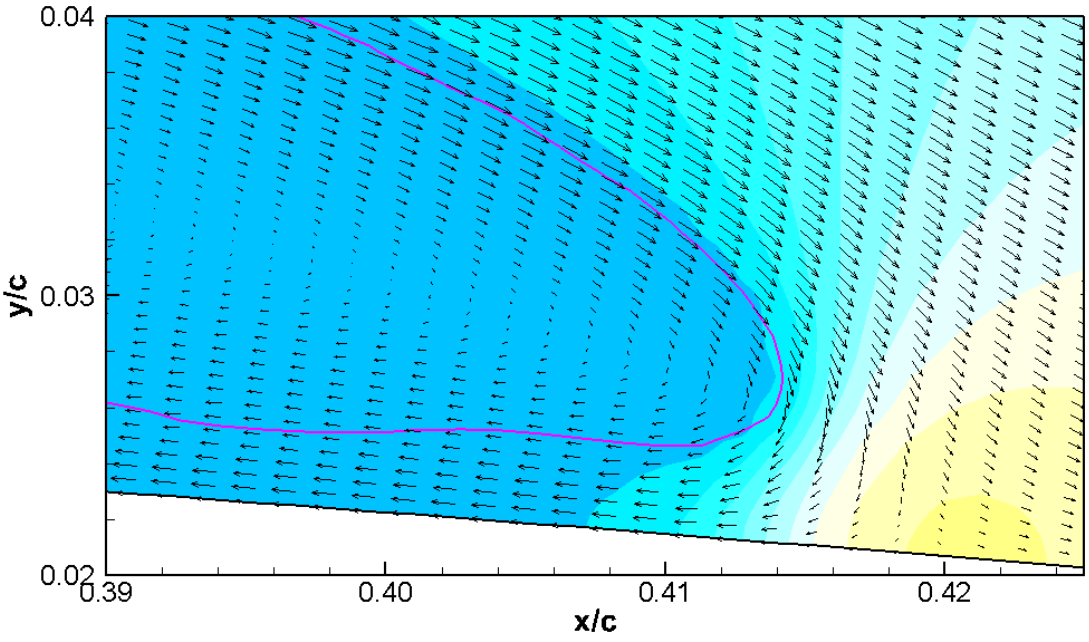

Figure 31: Trailing edge of cavity with stagnation point and reentrant jet.

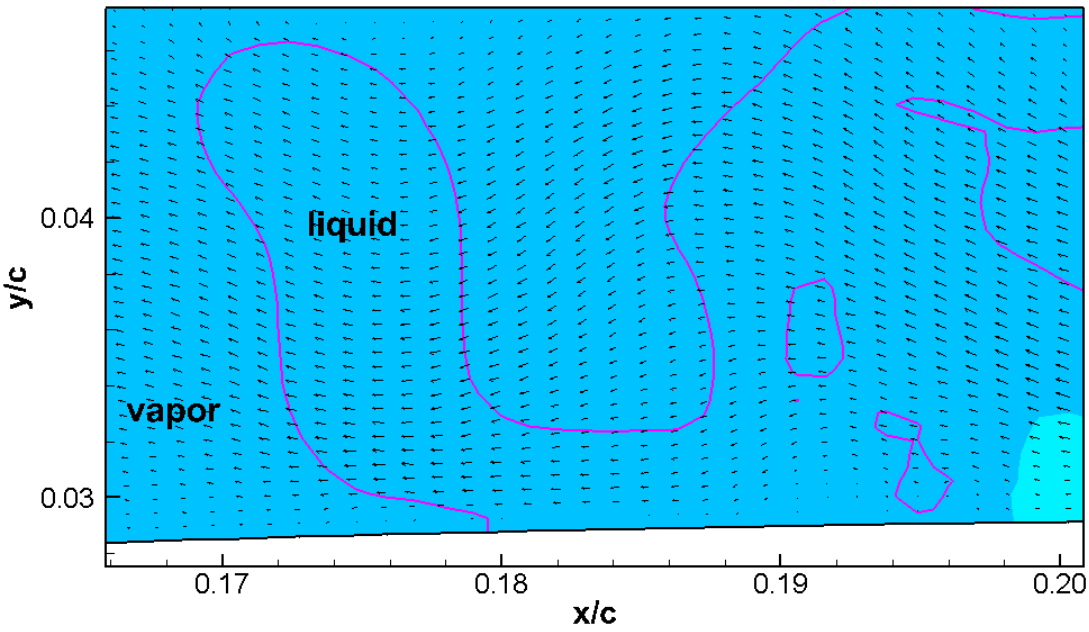

Figure 32: Forward front of reentrant jet.

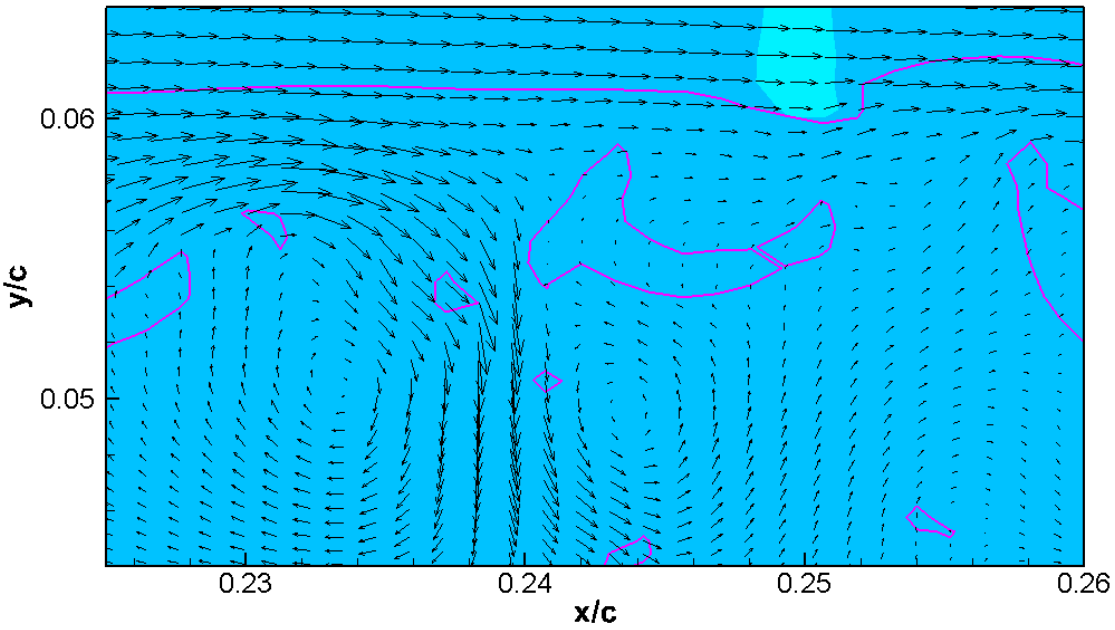

Figure 33: Complex flow in shedding region.

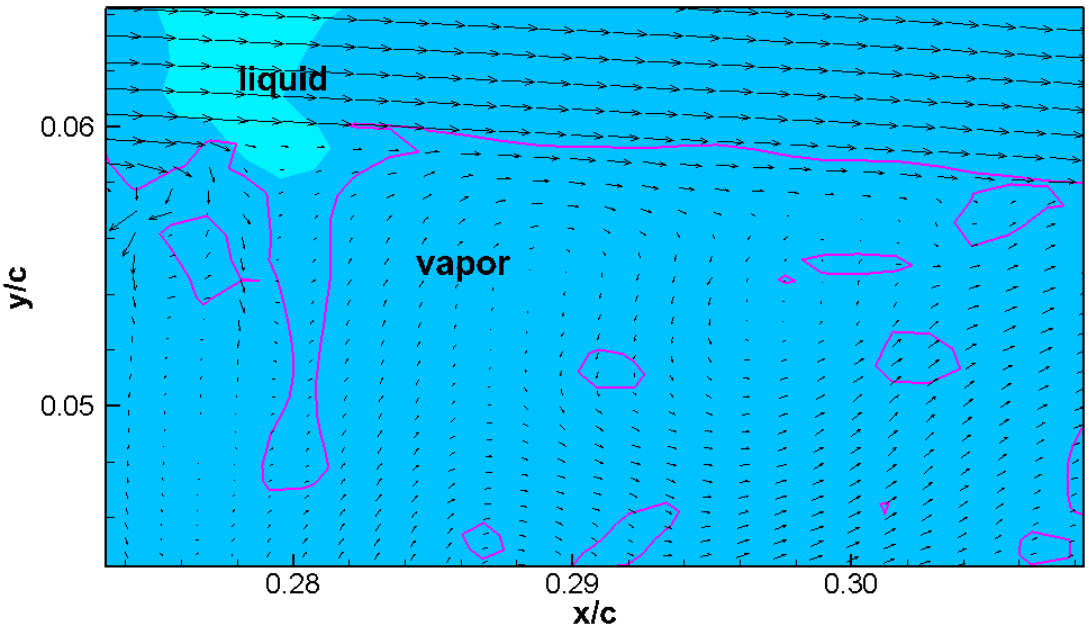

Figure 34: Droplets and destabilized interface in shedding region.

Figure 35 shows the leading edge of the cavity. The liquid flow appears to be tangent to the cavity. The relatively small normal component of the liquid velocity is not clearly visible. With a density approximately 50,000 times greater than the vapor, only a small amount of liquid needs to change phase as it crosses the interface to maintain the cavity.

A time series of the reentrant jet destabilizing the cavity is shown in Figure 36. A bump forms on the upper surface of the reentrant jet. This bump is unstable and forces a finger of liquid up into the cavity. Momentum carries the finger of liquid up toward the outer surface of the cavity. Simultaneously, the vapor velocity near the outer surface tries to drive the finger of liquid downstream. The vapor has relatively little momentum to impart to the liquid, and therefore not a very strong effect. The finger reaches the outer surface and disturbs it. In this case, the finger is relatively thin and fragments into droplets which are temporarily trapped in the vapor cavity. Eventually, enough droplets

accumulate in the cavity, or a strong enough finger reaches the outer surface to cause the aft part of the cavity to become separated from the main part of the cavity. Once the two parts are separated by a region with somewhat higher pressure, the aft part of the cavity will be shed downstream while the upstream part of the cavity begins to grow again.

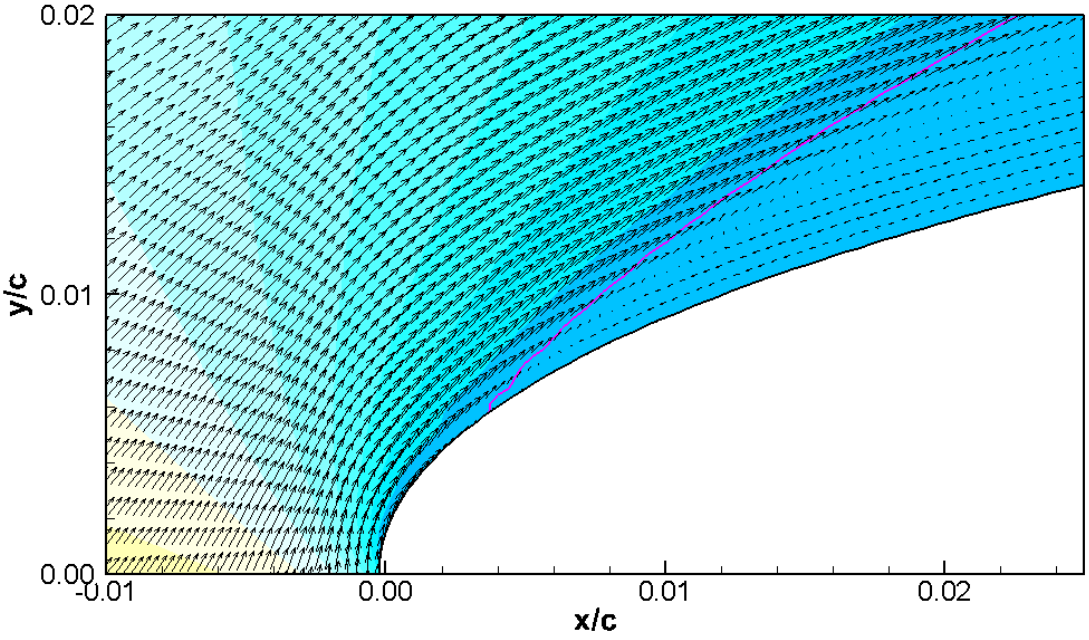

Figure 35: Leading edge of cavity with velocity vectors.

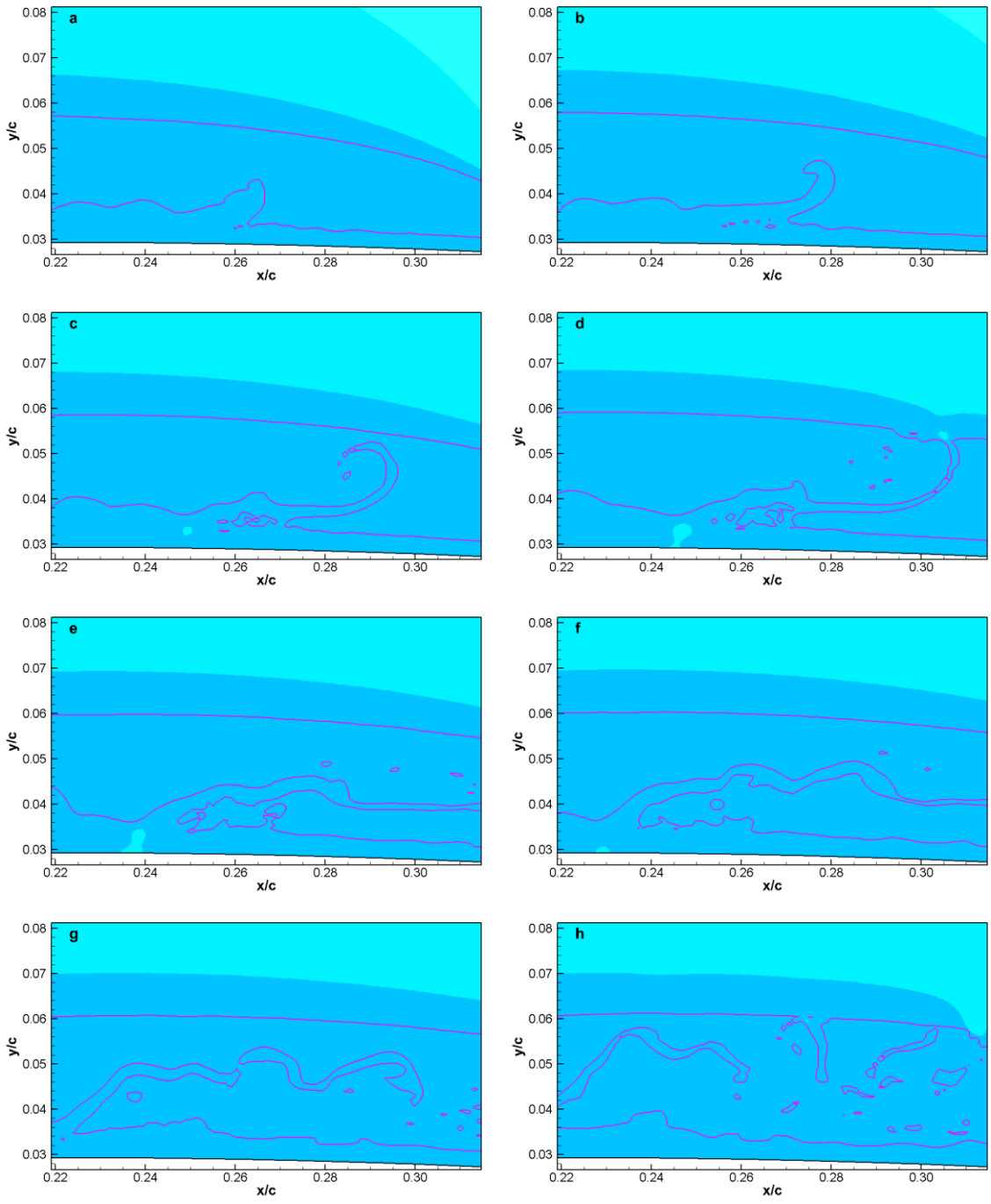

Figure 36: Time series of reentrant jet destabilizing cavity.

FUTURE WORK

Three Dimensions

An obvious future development would be the extension to three dimensions. This is already supported by the levelset and volume-of-fluid models. Since the directions are handled one-by-one, extension to three dimensions will be straight forward. Many provisions for the third dimension are included in the code.

The third dimension will allow better comparison with experiments. A particularly interesting case would be the Twist-11 hydrofoil (Foeth, 2008). In experiments using extruded foils, such as the experiment by Shen and Dimotakis (1989a, 1989b), the shedding location is random, making it difficult to study the shedding process. The Twist-11 foil was designed to produce cavity shedding in a specific location for studying and comparing with computations.

A third dimension will also allow modeling headforms, which are classic cavitating geometries.

Stability

The biggest fault of the current implementation is stability. Under-resolved bubbles, droplets, or very thin features, cause problems in the current implementation of the ghost fluid method. This leads to a poor intermediate velocity field, which requires large pressure excursions for the corrector step to satisfy continuity. The solution will likely consist of two parts: subgrid modeling for under-resolved features and improvements to the ghost fluid method. There are other reasons for subgrid modeling and it is discussed in more detail in a later section.

The philosophy of the current implementation of the ghost fluid method is to remove the normal velocity jump that occurs at the interface. This assumes that the expected velocity jump occurs in the flow field and relies on proper determination of the normal vector. When the flow field is extended into a small bubble, droplet, or thin

feature, the same velocity value must be used for all differences requiring a value at that point. The interface that is closest will be selected for determining the phase change rate and normal vector, which may be appropriate for every stencil using that point in a difference. For under-resolved features, a small movement of the interface may cause the direction of the normal to reverse as one interface becomes closer than the other.

Gibou *et al.* (2012) describe methods for implementing the ghost fluid method with a direction-by-direction method for constant, linear, or quadratic extrapolation. For velocity field extension, the authors follow the method described by Aslam (2003). In small droplets and bubbles and in thin features, different extrapolated velocities may result from each interface. This method requires modification to the advection code to build extrapolation into the method.

Tanguy *et al.* (2007) take a somewhat different approach and enforce a divergence free condition for the extended liquid velocity field. This is accomplished by solving a Poisson equation for the intermediate extended liquid velocity field. The extended gas velocity field does not receive the same treatment. The liquid velocity field is used for interface advection.

Schlottke and Weigand (2008) take a different approach and attempt to correct the combined intermediate velocity field by locating large divergences and altering the face velocities in a region to minimize the divergences. The method is applied direction-by-direction and cells containing the most liquid are corrected first. This pushes the error into the cells containing the most gas. Because the gas has less momentum for the same velocity, a smaller pressure excursion will result than if the error were in a predominantly liquid cell.

Subgrid Model

Sharp interface models can only accurately resolve bubbles and droplets larger than the local mesh size. Surface tension may prevent the splitting of small droplets and

bubbles. However, phase change can cause droplets and bubbles to shrink and disappear as their mass is converted to the other phase. So, no matter how fine the grid is, a bubble or droplet can become smaller than the grid.

A subgrid model would also benefit cavitation inception modeling. Currently, a bubble must occupy several cells to be resolved. So, rather than growing from a nuclei, bubbles appear suddenly and create a strong disturbance in the solution.

In the study of atomization, the flow from a jet can be divided into three regimes: one, the initial jet flow, suitable for sharp interface modeling; two, the large droplets, suitable for a discrete bubble model; and three, the tiny droplets, suitable for a mixture model. These same categories can be applied to cavitation. However, there is a distinct difference in that with spray the conversion is typically only from large scale to small scale. With cavitation, bubbles and droplets will need to be converted in both directions.

Herrmann (2006, 2010) presents a method for identifying small droplets and ligaments (thin liquid features) utilizing the level set method. Once identified, these features can be transfered to the subgrid model. The next step for cavitation modeling is to implement the identification of these features. For transfer in the reverse direction, discrete bubbles which reach a radius larger than one cell can be transferred to the sharp interface model.

To properly model both the liquid and the vapor, discrete bubbles and droplets may both need to be tracked, with the sharp interface model and homogenous mixture models shared between the two phases. Simple models can be used for the collision and breakup of large droplets and bubbles.

Calibration of the Model

Additional parametric studies including the NACA 0015 hydrofoil cases used by several other researchers (Hosangadi and Ahuja, 2005; Kim and Brewton 2008; Koop, 2008) and sharp orifice cases like those used by Singhal *et al.* (2002) can be used to

determine generally applicable values for the evaporation and condensation coefficients. Additional cases that may be useful are the injectors often computed by Yuan and Schnerr (*eg*. 2003) and the venturi tested and computed by Goncalves *et al.* (2010). A dynamically pitching Joukowski foil was tested by Shen and Peterson (1978). The X-ray experiments by Mäkiharju *et al.* (2012) provide some insight into the fraction of liquid in the cavity which could be compared with the calculations from this model.

Inert Gasses

Liquid water typically contains some dissolved air. The air tends to leave the solution and enter the vapor bubbles. This increases the size of the bubbles and results in a new minimum size since the air will not easily go back into solution. Accounting for this, as in the model developed by Singhal *et al*. (2002), would be a logical future development. To do this in the context of the sharp interface model will require the use of a mixture model within the bubbles. The implementation of a mixture model that follows the sharp interface and conserves the air mass while allowing for phase change of the water will be challenging.

CONCLUSIONS

A sharp interface cavitation model has been developed. This includes a model for the mass flux between phases which was derived from the Rayleigh-Plesset equation. The phase change rate is computed semi-implicitly by incorporating it into the solution of the Poisson equation for pressure. A ghost fluid method was added to permit a normal velocity jump at the interface with the existing momentum solution method. A flux-jump method was developed as an improvement on discrete velocity jumps for handling the effect of the volume source at the interface.

The flux jump method builds on the discrete velocity jump methods applied with the level set function by Nguyen *et al.* (2001), Son and Dhir (2007), and Gibou *et al.* (2007). The new method adds surface area information from the VOF model to create and integral form of the method. This improvement is particularly significant near solid boundaries.

Several two-dimensional bubble problems were solved to demonstrate the methods applicability to surface cavitation on a hydrofoil. The development of a method to identify and apply corrections for small bubbles and droplets remains to be completed.

Surface cavitation on a NACA 66 hydrofoil has been computed and compared with experimental data. The sharp interface technique shows the ability to provide insight into the details of surface cavitation on foils. Further development to improve stability, and extension to a three-dimensional model, and the computation of the associated large grids, will be necessary to better match the experimental measurements.

REFERENCES

Abbot, I.H., and A.E. Von Doenhoff. 1959. *Theory of Wing Sections*. New York: Dover.

Arndt, R.E.A., G.J. Balas, and M. Wosnik. 2005. Control of cavitating flows: A perspective. *JSME International Journal, Series B*, 48(2):334-341.

Aslam, T.D. 2003. A partial differential equation approach to multidimensional extrapolation. *Journal of Computational Physics*, 193:349–355.

Bensow, R.E., T. Huuva and G. Bark. 2008. Large eddy simulation of cavitating propeller flows. *27th Symposium on Naval Hydrodynamics*, 5-10 October, Seoul, Korea.

Ceverone, A., C. Bramanti, E. Rapposelli, L. d'Agostino. 2006. Thermal cavitation experiments on a NACA 0015 hydrofoil. *Journal of Fluids Engineering*. 128:326-331.

Delannoy Y, Kueny JL> 1990. Two-phase flow approach in unsteady cavitation modeling. Cavitation and Multiphase Flow Forum, ASME-FED 98, 153-158.

Falgout, R.D., J.E. Jones, and U.M. Yang. 2006. The design and implementation of HYPRE, library of parallel high performance preconditioners. *Numerical Solution of Partial Differential Equations on Parallel Computers*. A.M. Bruaset and A. Tveito, eds. Springer-Verlag. 51:267-294.

Fedkiw, R.P., T. Aslam, B. Merriman, and S. Osher. 1999a. A Non-oscillatory Eulerian approach to interfaces in multimaterial flows (the ghost fluid method). *Journal of Computational Physics*, 152:457-492.

Fedkiw, R.P., T. Aslam, and S. Xu. 1999b. The ghost fluid method for deflagration and detonation discontinuities. *Journal of Computational Physics*, 154:393-427.

Foeth, E.J., C.W.H. van Doorne, T. van Terwisga, and B. Wieneke. 2006. Time resolved PIV and flow visualization of 3D sheet cavitation. *Experiments in Fluids*, February, 40:503-513.

Foeth, E.J. 2008. *The Structure of Three-dimensional Sheet Cavitation*. Ph.D. dissertation, Delft University of Technology.

Foeth, E.J., T. van Terwisga, and C. van Doorne. 2008. On the collapse structure of an attached cavity on a three-dimensional hydrofoil. *Journal of Fluids Engineering*, June, 130:071303.

Franc, J.-P. and J.-M. Michel. 2004. *Fundamentals of Cavitation*. Dordracht: Kluwer Academic Publishers.

Gibou, F., L. Chen, D. Nguyen, and S. Banerjee. 2007. A level set based sharp interface method for the multiphase incompressible Navier-Stokes equations with phase change. *Journal of Computational Physics*, 222:536-555.

Gibou, F., C. Min, R. Fedkiw. 2012. High resolution sharp computational methods for elliptic and parabolic problems in complex geometries. *Journal of Scientific Computing*, 54:369–413.

Goncalves, E., M. Champagnac, and R. Fortes Patella. 2010. Comparison of numerical solvers for cavitating flows. *International Journal of Computational Fluid Dynamics*, 24:201-216.

Herrmann, M. 2003. A domain decomposition parallelization of the fast marching method. *Center for Turbulence Research Annual Research Briefs*. 213-225.

Herrmann, M. 2006. Simulating two-phase flows using the refined level set grid method. ILASS Americas 19th Annual Conference on Liquid Atomization and Spray Systems, Toronto, Canada.

Herrmann, M. 2010. A parallel Eulerian interface tracking/Lagrangian point particle multi-scale coupling procedure. *Journal of Computational Physics*, 229:745-759.

Hosangadi, A. and V. Ahuja. 2005. A new unsteady model for dense cloud cavitation. *Proceedings of FEDSM2005*, June 19-23, Houston, TX, USA.

Kang, S., G. Iaccarino, F. Ham, and P. Moin. 2009. Prediction of wall-pressure fluctuation in turbulent flows with an immersed boundary method. *Journal of Computational Physics*. 228:6753-6772.

Kato, H., T. Maeda, and A. Magaino. 1978. Mechanism and scaling of cavitation erosion. *Proceedings of the 12th ONR Symposium on Naval Hydrodynamics*, 452-469.

Kim, S.-E. and S. Brewton. 2008. A multiphase approach to turbulent cavitating flows. *Proceedings of the 27th Symposium on Naval Hydrodynamics*, Seoul, Korea, October 5-10.

Kim, S.-E., S. Schroeder and H. Jasak. 2010a. A multi-phase CFD framework for predicting performance of marine propulsors. *The 13th International Symposium on Transport Phenomena and Dynamics of Rotating Machinery*, Honolulu, Hawaii, USA, April 4-7.

Kim, S.-E. and S. Schroeder. 2010b. Numerical study of thrust-breakdown due to cavitation on a hydrofoil, a propeller, and a waterjet. *Proceedings of the 28th Symposium on Naval Hydrodynamics*, Pasedena, California, USA, 12-17 September.

Kerwin, J.E. , S.A. Kinnas, J.-T. Lee, and W.-Z. Shih. 1987. A surface panel method for the hydrodynamic analysis of ducted propellers. *SNAME Transactions*, 95:93-122.

Kjeldsen, Morten, R.E.A. Arndt, and M. Effertz. 2000. Spectral characteristics of sheet/cloud cavitation. *Journal of Fluids Engineering*. 122:481-487.

Koop, A.H. 2008. *Numerical Simulation of Unsteady Three-Dimensional Sheet Cavitation*. University of Twente.

Kubota, A., H. Kato and H. Yamaguchi. 1992. A new modelling of cavitating flows: A numerical study of unsteady cavitation on a hydrofoil section. *Journal of Fluid Mechanics*, 240:59-96.

Kunz, R.F., D.A. Boger, T.S. Chyczewski, D.R. Stinebring, and H.J. Gibeling. 1999. Multi-phase CFD analysis of natural and ventilated cavitation about submerged bodies. Proceedings of FEDSM '99, 3rd ASME/JSME Joint Fluids Engineering Conference.

Kuiper, G. 1981. *Cavitation Inception on Ship Propeller Models*. Ph.D. dissertation, Technical University of Delft.

Lee, C.-S. 1979. *Prediction of Steady and Unsteady Performance of Marine Propellers With or Without Cavitation by Numerical Lifting Surface Theory*. Ph.D. dissertation, Massachusetts Institute of Technology.

Li, D., and C.L. Merkle. 2006. A unified framework for incompressible and compressible fluid flows. *Journal of Hydrodynamics Ser. B.* 18:113-119.

Mäkiharju, S., M. Perlin, and S.L. Ceccio. 2012. Time resolved x-ray densitometry for cavitating and ventilated partial cavities. 29th Symposium on Naval Hydrodynamics, Gothenburg, Sweden, August 26-31.

Merkle, C. L., J.Z. Feng and P.E.O. Buelow. 1998. Computational modeling of the dynamics of sheet cavitation. Third International Symposium on Cavitation, Grenoble, France, April 7-10.

Nguyen, D.Q., R.P. Fedkiw, and M. Kang. 2001. A boundary condition capturing method for incompressible flame discontinuities. *Journal of Computational Physics*. 172:71-98.

Plesset, M.S. and A. Prosperetti. 1977. Bubble dynamics and cavitation. *Annual Review of Fluid Mechanics*, 9:145-185.

Schlottke, J. and B. Weigand. 2008. Direct numerical simulation of evaporating droplets. *Journal of Computational Physics*, 227(10):5215–5237

Senocak, I., and W. Shyy. 2004a. Interfacial dynamics-based modelling of turbulent cavitating flows, Part-1: Model development and steady-state computations. *International Journal for Numerical Methods in Fluids*, 44:975-995.

Senocak, I., and W. Shyy. 2004b. Interfacial dynamics-based modelling of turbulent cavitating flows, Part-2: Time dependent computations. *International Journal for Numerical Methods in Fluids*, 44:997-1016.

Shen, Y.T. and P.E. Dimotakis. 1989a. The influence of surface cavitation on hydrodynamic forces. 22nd American Towing Tank Conference, St Johns, Newfoundland, Canada, August 8-11.

Shen, Y.T. and P.E. Dimotakis, 1989b. Viscous and nuclei effects on hydrodynamic loadings and cavitation of a NACA 66 (mod) foil section. *Transactions of the ASME*, 111:306-316.

Shen, Y.T. C.W. Jiang, and K.D. Remmers. 1997. A twisted rudder for reduced cavitation. *Journal of Ship Research*. 41(4):260-272.

Shen, Y.T. and F.B. Peterson. 1978. Unsteady cavitation on an oscillating hydrofoil. 12th Symposium on Naval Hydrodynamics, Washington D.C, 362-384.

Singhal, A.K., M.M. Athavale, H. Li, and Y. Jiang. 2002. Mathematical basis and validation of the full cavitation model. *Journal of Fluids Engineering*. 124:617-624.

Son, G. and V.K. Dhir. 2007. A level set method for analysis of film boiling on an immersed solid surface. *Numerical Heat Transfer, Part B: Fundamentals*, 52: 153-177.

Suh, J., J. Yang, F. Stern. 2011. The effect of air-water interface on the vortex shedding from a vertical circular cylinder. *Journal of Fluids and Structures*, 27:1-22.

Tanguy, S., T. Menard, and A. Berlemont. A level set method for vaporizing two phase flows. *Journal of Computational Physics*, 221:837-853.

Wang, Z., J. Yang, B. Koo, and F. Stern. 2009. A coupled level set and volume-of-fluid method for sharp interface simulation of plunging breaking waves. *International Journal of Multiphase Flow*. 35:227-246.

Wang, Z., J. Yang, and F. Stern. 2012. A new volume-of-fluid method with a constructed distance function on general structured grids. *Journal of Computational Physics*. submitted for publication.

Wosnik, M. and I. Milosevic. 2005. Time-resolved particle image velocimetry (TR-PIV) in ventilated and naturally cavitating flows. Sixth International Symposium on Particle Image Velocimetry, Pasedena, California, USA, September 21-23.

Yang, J.,S. Bhushan, J.S. Suh, Z. Wang, B. Koo, N. Sakamoto, T. Xing, and F. Stern. 2008. Large-eddy simulation of ship flows with wall-layer models on Cartesian grids. Proceedings of the 27th Symposium on Naval Hydrodynamics, Seoul, Korea.

Yang, J. and F. Stern. 2009. Sharp interface immersed-boundary/level-set method for wave-body interactions. *Journal of Computational Physics*. 228:6590-6616.

Yang, J. and F. Stern. 2011. A simple and efficient parallel implementation of the fast marching method. The 64th Annual Meeting of the American Physical Society - Division of Fluid Dynamics, Baltimore, Maryland.

Yuan, W. and G. Schnerr. 2003. Numerical simulation of two-phase flow in injection nozzles: interaction of cavitation and external jet formation. *Journal of Fluids Engineering,* 125(6), 963-969